ORIGINAL ARTICLE

# Combined phase diagram modelling and quartz-in-garnet barometry of *HP* metapelites from the Kamieniec Metamorphic Belt (NE Bohemian Massif)

Jacek Szczepański[1] (iD)    |    Xin Zhong[2,3] (iD)    |    Marcin Dąbrowski[3,4] (iD)    |    Haozheng Wang[5]    |    Marcin Goleń[1]

[1]Institute of Geological Sciences, University of Wroclaw, Wrocław, Poland

[2]Institute of Geological Sciences, Freie Universität Berlin, Berlin, Germany

[3]Physics of Geological Processes, The Njord Centre, University of Oslo, Oslo, Norway

[4]Computational Geology Laboratory, Polish Geological Institute – National Research Institute, Wrocław, Poland

[5]School of Geoscience and Technology, Southwest Petroleum University, Chengdu, China

**Correspondence**
Jacek Szczepański, Institute of Geological Sciences, University of Wroclaw, Wrocław, Poland.
Email: jacek.szczepanski@uwr.edu.pl

**Funding information**
Narodowe Centrum Nauki, Grant/Award Number: UMO-2015/17/B/ST10/02212

**Handling Editor:** Richard White

## Abstract

The Kamieniec Metamorphic Belt belongs to the Variscan Belt of Europe as the NE part of the Bohemian Massif. It comprises a supracrustal succession dominated by micaschists that has not been yet recognized as a high-*P*, low-*T* (*HP–LT*) metamorphic unit. Our work demonstrates the significance of metapelites in the study of *HP* metamorphism of the NE part of the Bohemian Massif. To reconstruct the *P–T* history of the Kamieniec Metamorphic Belt, we have investigated three samples using independent geothermobarometric techniques including phase diagram modelling, $Si^{4+}$ content in white mica and quartz-in-garnet elastic barometry. Two samples contain mineral assemblages bearing a record of *HP* metamorphism followed by an *LP* event. The oldest assemblage is mostly preserved in the first generation of garnet and it comprises phengitic white mica and rutile. In one of the investigated samples, we also recognized chloritoid and inferred pseudomorphs after lawsonite composed of quartz, clinozoisite associated with margarite. The third of the investigated samples is strongly retrogressed and only contains the relics of phengitic white mica. All three samples contain a younger mineral assemblage comprising white mica with low $Si^{4+}$ content and ilmenite. Mineral equilibria modelling indicates the *P–T* conditions of the *HP* event culminated at ~15.5–18 kbar and ~470–570℃, while the *LP* episode occurred at ~5–7 kbar and ~530–570℃. The Raman shift measured in quartz inclusions in garnet in samples with a well-preserved record of the *HP* stage points to their entrapment at pressures between 11 and 16 kbar. The quartz inclusions within the strongly retrogressed micaschist sample exhibit Raman shifts corresponding to the *LP* episode at ~5–8 kbar. Discrepant results obtained for one of the samples are discussed in detail. Our investigations show that the supracrustal succession of the Kamieniec Metamorphic Belt contains a record of *HP–LT* metamorphism typical for subduction systems. A recently established tectonic model for the crystalline complexes exposed in the Bohemian Massif suggests that they were formed via the collision of the Saxothuringian, Teplá–Barrandian, and Brunovistulian domains.

Therefore, we interpret the Kamieniec Metamorphic Belt as representing fragments of the Saxothuringian crust that experienced cold extrusion from below the Teplá–Barrandian domain in front of the rigid Brunovistulian indenter.

## 1 | INTRODUCTION

Numerous occurrences of high-*P*, low-*T* (*HP–LT*) terranes within collisional orogenic belts indicate that the exhumation of subducted continental crust is a natural consequence of the continental collision. The exact mechanism of exhumation can be deciphered by studying the metamorphic conditions recorded within the exhumed fragments of the subducted continental crust. The common mineral assemblages in supracrustal successions related to *HP–LT* metamorphism involve chloritoid, phengite, and lawsonite (e.g. Aguilar et al., 2020; Martin et al., 2014; Negulescu et al., 2009; Tsuchiya & Hirajima, 2013). However, these minerals are often prone to later metamorphic overprint and may be poorly preserved in exhumed rock complexes. For example, lawsonite, which has been reported from several *HP–LT* terranes including, for example, the Cyclades (Philippon et al., 2013), Sanbagawa metamorphic belt (Ueno, 2001), and Tian Shan (Orozbaev et al., 2015), is rarely preserved during retrograde metamorphism, predominantly surviving in the form of pseudomorphs (e.g. Hamelin et al., 2018; Orozbaev et al., 2015). In some cases, the growth of lawsonite can only be deduced from mineral equilibria modelling (e.g. Cruciani et al., 2013). Despite its poor preservation potential, owing to the diagnostic *P–T* conditions of its formation, lawsonite may be used as a proxy for tracing palaeo-subduction zones, which precede collisional events leading to the formation of orogenic belts (e.g. Poli & Schmidt, 1995; Tsujimori & Ernst, 2014). As phengite and chloritoid are more often preserved as either inclusions or matrix minerals (e.g. Chu et al., 2009; Negulescu et al., 2009), their occurrences, corroborated by the presence of lawsonite pseudomorphs, may serve as a good indicator of *HP* and *LT* metamorphism.

The Variscan Belt of Europe extends from the Iberian Massif in the SW to the Bohemian Massif in the NE, and is a result from collisional events related to the convergence between the Gondwana and Laurussia plates, including the entrapped Armorican Terrane Assemblage (e.g. Franke et al., 2017). This collage of metamorphic terranes was formed during Devonian to Carboniferous times. Reconstructing the geodynamic evolution of an orogenic belt largely builds on the recognition of fossil subduction zones, which often preserve records of *HP–LT* metamorphism. Recently, several such metamorphic terranes have been recognized in various sectors of the Variscan Belt of Europe, including the Saxothuringian of the Bohemian Massif (e.g. Jeřábek et al., 2016).

In this paper, we examine the micaschists from the Kamieniec Metamorphic Belt (KMB), located within the NE Bohemian Massif in Poland. We describe, for the first time, the occurrence of *HP–LT* metamorphism in this part of the Variscan Belt of Europe. To document *HP–LT* metamorphism, we use a combined approach that includes phase diagram modelling, conventional geothermobarometry including Si$^{4+}$ content in white mica and pressure estimates based on the Raman shift of quartz inclusions in garnet. Furthermore, chloritoid inclusions and highly phengitic composition of some white mica along with presumed pseudomorphs after lawsonite supports the *HP* history of the inspected samples. The new results on the pressure and temperature history of the *HP–LT* micaschists of the KMB are discussed in the framework of tectonic models for the NE sector of the Variscan Belt of Europe.

## 2 | GEOLOGICAL BACKGROUND

Metamorphic complexes in the Bohemian Massif have been interpreted as resulting from the long-lasting, Andean-type convergence of the Saxothuringian, Teplá–Barrandian, and Brunovistulian domains (e.g. Schulmann et al., 2009). However, unravelling the history of the north-easternmost fragment of the Variscan Belt of Europe, and in particular the Fore-Sudetic Block, is made difficult by scarce outcrops of crystalline rocks, which, particularly within the Fore-Sudetic Block, only locally emerge from below the Mesozoic and Cenozoic cover (Figure 1). The KMB (Figure 1) is one of the most easterly located exposures of crystalline rocks in the Variscan Belt of Europe. This part of the Fore-Sudetic Block comprises fragments of the East and Central Sudetes, which are interpreted as belonging to the Brunovistulian and Saxothuringian crustal domains respectively (e.g. Aleksandrowski & Mazur, 2002; Franke et al., 1993; Mazur et al., 2015; Oberc-Dziedzic et al., 2003; Oberc-Dziedzic et al., 2018; Schulmann & Gayer, 2000). Micaschists with small intercalations of felsic and mafic metavolcanics, paragneisses, quartzites, graphite schists, marbles, and eclogites are predominantly exposed in the KMB (Figure 1b and c).
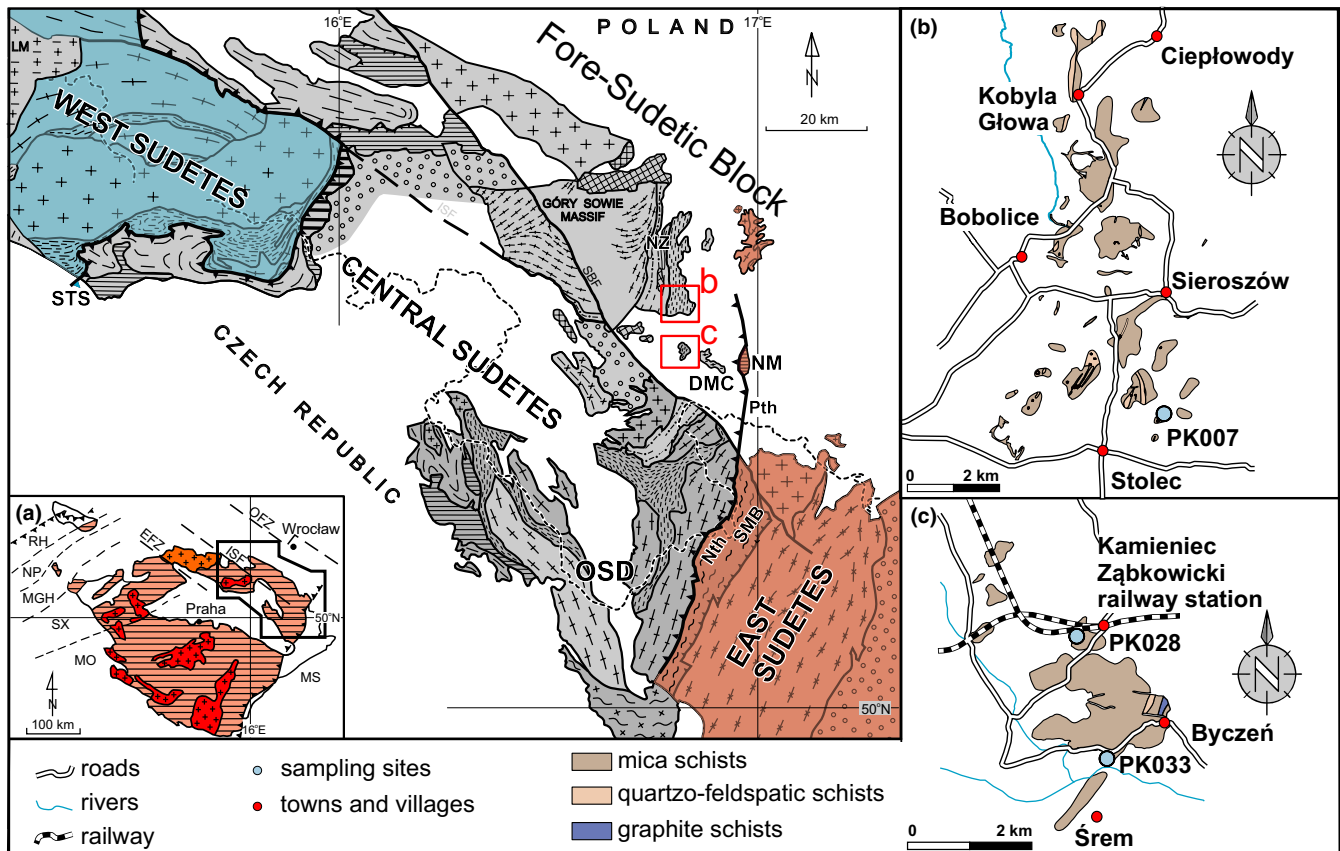
**FIGURE 1** Geological sketch map of the Sudetes after Mazur et al., (2005). The inset a shows the location of the study area within the Bohemian Massif. Insets b and c show geological sketch maps of the northern (b) and central (c) part of the Kamieniec Metamorphic Belt with samples location marked. Abbreviations: NM, Niedźwiedź massif; DMC, Doboszowice Metamorphic Complex; NZ, Niemcza shear zone; Pth – Paczków thrust; Nth – Nýznerov thrust; OSD, Orlica–Śnieżnik dome; SBF, Sudetic Boundary Fault; ISF, Intra-Sudetic fault; SMB, Staré Město belt; STS, Saxo-Thuringian suture. Abbreviations in inset a: MGH, Mid-German Crystalline High; MO, Moldanubian zone; OFZ, Odra Fault Zone; MS, Moravo-Silesian zone; NP, Northern Phyllite zone; RH, Rhenohercynian zone; SX, Saxothuringian zone; EFZ, Upper Elbe fault Zone, ISF, Intra-Sudetic fault

Based on micropaleontological evidence, Neoproterozoic to Cambrian age was established for the protolith of this supracrustal succession (Gunia et al., 1979). This is in agreement with the protolith age of an orthogneiss from the neighbouring Doboszowice Metamorphic Complex (Figure 1), which intruded the volcano-sedimentary succession at 488.4 ± 6.2 Ma (Mazur et al., 2010). It is also confirmed by recently published results of detrital zircon geochronology of micaschists from the KMB suggesting latest Neoproterozoic maximum age of deposition of these rocks (Jastrzębski et al., 2020). The whole succession was deformed and metamorphosed during the Variscan collision of the Brunovistulian and Saxothuringian microplates (Mazur & Józefiak, 1999; Mazur & Puziewicz, 1995).

The age of metamorphism and related deformation is constrained in the central part of the Fore-Sudetic Block by $^{40}$Ar–$^{39}$Ar dating of hornblende, yielding $c$. 376 Ma and 331.9 ± 1.7 Ma for hornblende-bearing rocks from the Kamieniec Metamorphic Belt and the neighbouring Niemcza Shear Zone respectively (Steltenpohl et al., 1993).

Furthermore, chemical U–Th–total Pb electron probe microanalysis (EPMA) monazite geochronology data indicate an important regional tectono-metamorphic event at $c$. 330 Ma (Jastrzębski et al., 2020). The volcano-sedimentary succession of the KMB was intruded by syntectonic granitoids. Similar rocks, exposed in the neighbouring Niemcza Shear Zone, have been dated at $c$. 340–330 Ma by U–Pb and Pb–Pb methods on zircons (Oliver et al., 1993; Pietranik et al., 2013). Therefore, the Variscan tectonothermal activity in this area covers a time span from $c$. 376 Ma to $c$. 330 Ma.

The metamorphic record in the KMB has been studied by means of conventional geothermobarometry (Dziedzicowa, 1973; Dziedzicowa, 1987; Nowak, 1998 and Józefiak, 2000). Nowak (1998) investigated rocks in the vicinity of Kamieniec Ząbkowicki and demonstrated that garnetiferous micaschists contained a record of a clockwise $P$–$T$ path with a peak pressure of 11–12 kbar at 400–430℃, followed by a temperature peak of ~580℃ at ~7.5 kbar. Józefiak (2000) estimated peak metamorphic conditions preserved in micaschists at ~540–590℃ and ~7.5–10.5 kbar.

However, Józefiak (2000) postulated even higher *P–T* conditions, in the range from 610 to 630℃ and from 10 to 13 kbar, for micaschists enveloping eclogites. The peak metamorphic event was followed by decompression to ~3–5 kbar and ~550℃ (Józefiak, 2000; Nowak, 1998). Nowak (1998) documented rare occurrences of lawsonite pseudomorphs preserved in garnet grains from micaschists of the KMB. Moreover, Achramowicz et al. (1997) and Bakun-Czubarow (1998) described eclogite lenses exposed in the southern part of the KMB, with preserved mineral assemblages pointing to metamorphism at ~575℃ and ~15 kbar. Therefore, we have performed new phase diagram modelling combined with quartz-in-garnet elastic barometry to resolve the discrepancy between the *P–T* conditions deciphered from eclogite lenses and surrounding, presumably lawsonite pseudomorph-bearing micaschists of the KMB.

According to Mazur and Józefiak (1999), the Kamieniec Metamorphic Belt, together with the neighbouring Doboszowice Metamorphic Complex, comprises refolded tectonic units interpreted as a nappe pile. The base of the refolded nappe pile is defined by the Paczków thrust, which separates it from the underlying metabasites of the Niedźwiedź Massif (Mazur & Józefiak, 1999). It is believed that the Paczków thrust represents a northern continuation of the Nýznerov thrust, separating the metamorphic complexes of the Central and East Sudetes (Skacel, 1989) and in terms of crustal domains the Brunovistulian and Saxothuringian microplates(Figure 1).

# 3 | SAMPLES AND METHODS

To characterize the metamorphic history of the studied micaschists from the KMB, we conducted a detailed study of three samples. Sample PK007 was collected in the northern part of the study area, in the vicinity of Stolec (Figure 1b), while samples PK028 and PK033 were collected from the southern part of the KMB, in the vicinity of Kamieniec Ząbkowicki (Figure 1c). The bulk rock compositions of the samples were obtained from inductively coupled plasma mass spectrometry (ICP-MS) analysis and are presented in Table 1.

Mineral analyses were carried out at the Inter-Institutional Analytical Laboratory for Minerals and Synthetic Substances, Faculty of Geology, University of Warsaw, using a Cameca SX100 electron microprobe equipped with four wavelength-dispersive spectrometers. Standard operating conditions were: acceleration voltage 15 kV, beam current 10 nA (muscovite, biotite, chlorite, feldspars, staurolite, garnet), 20 nA (ilmenite), and beam diameter ~3–5 μm. Natural and synthetic silicate and oxide minerals were used for calibration. The microprobe data were normalized and formulae were calculated as follows: for biotite and muscovite to 12 oxygens

**TABLE 1** Bulk rock composition of the studied samples from the KMB determined with ICP-MS spectrometry

| Sample | PK007 | PK028 | PK033 |
|---|---|---|---|
| $SiO_2$ | 62.41 | 51.65 | 61.56 |
| $Al_2O_3$ | 19.41 | 22.96 | 19.72 |
| $Fe_2O_3$ | 6.69 | 10.57 | 6.97 |
| MgO | 1.68 | 1.92 | 1.69 |
| CaO | 0.57 | 1.41 | 0.61 |
| $Na_2O$ | 1.10 | 1.76 | 0.83 |
| $K_2O$ | 3.51 | 6.06 | 3.98 |
| $TiO_2$ | 0.85 | 1.05 | 1.08 |
| $P_2O_5$ | 0.12 | 0.07 | 0.19 |
| MnO | 0.34 | 0.15 | 0.18 |
| $Cr_2O_3$ | 0.01 | 0.014 | 0.02 |
| LOI | 3.10 | 2.10 | 2.90 |
| Sum | 99.79 | 99.71 | 99.73 |

(total Fe as FeO), for garnet to 12 oxygens (total Fe as FeO), for chlorite to 14 oxygens (total Fe as FeO), for chloritoid and feldspars to 8 oxygens, for staurolite to 46 oxygens, for epidote for 12.5 oxygens (total Fe as $Fe_2O_3$), for ilmenite to 3 oxygens and to 2 cations ($Fe^{3+}$ was estimated following the procedure of Droop, 1987). All mineral abbreviations are after Whitney and Evans (2010), while the abbreviation p.f.u. denotes per formula unit. Abbreviations for garnet species are: $X_{alm} = [Fe/(Ca + Fe + Mg + Mn)] * 100$, $X_{prp} = [Mg/(Ca + Fe + Mg + Mn)] * 100$, $X_{grs} = [Ca/(Ca + Fe + Mg + Mn)] * 100$, $X_{sps} = [Mn/(Ca + Fe + Mg + Mn)] * 100$. Albite content in plagioclase is calculated as $X_{Ab} = [Na/(Ca + Na + K)] * 100$. $X_{Mg}$ in staurolite, chloritoid, and biotite is calculated as $= Mg/(Fe + Mg)$. Representative chemical analyses of mineral phases are presented in Tables 2–8. Element-distribution maps of garnet grains were generated using WDS stage scans for Fe, Mg, Ca, and Mn. The mapping was conducted with a focussed beam using step sizes of 2–10 μm, beam currents of 50–200 nA, and dwell times of 30–50 ms. X-ray chemical maps for samples PK007 and PK033 were measured at the Laboratory of Scanning Electron Microscopy, Institute of Geological Sciences, University of Wrocław, using JEOL JSM-IT500LA. X-ray chemical maps for sample PK028 were obtained at the Inter-Institutional Analytical Laboratory for Minerals and Synthetic Substances, Faculty of Geology, University of Warsaw, using a ZEISS SIGMA VP.

*P–T* paths for the investigated samples were calculated using the bulk rock compositions, garnet crystal chemistry, and the semi-automated routine of Moynihan and Pattison (2013). The method includes several steps:

1. calculation of an isochemical phase diagram for bulk rock compositions,

**TABLE 2**  Representative EMP analyses of garnet grains in investigated micaschists (oxides in wt.%, cation in a pfu). $X_{Fe}$ = Fe/(Fe + Mg)

| Sample | PK007 | PK007 | PK007 | PK007 | PK007 | PK007 | PK028B | PK028B | PK028B | PK028B | PK028B | PK028B | PK028B | PK028B | PK033 | PK033 | PK033 |
|---|---|---|---|---|---|---|---|---|---|---|---|---|---|---|---|---|---|
| Profile | 4 | 4 | 4 | 6 | 6 | 6 | 5 | 5 | 5 | 5 | 5 | 5 | 5 | 5 | 3 | 3 | 3 |
| Point | rim | core | rim | rim | core | rim | outer rim | inner rim | mantle | core | mantle | core | outer rim | outer rim | rim | core | rim |
| SiO$_2$ | 36.95 | 36.75 | 36.80 | 36.73 | 36.43 | 36.78 | 37.80 | 37.53 | 37.56 | 37.16 | 37.28 | 37.17 | 37.44 | 37.91 | 37.42 | 37.22 | 37.24 |
| TiO$_2$ | 0.07 | 0.18 | 0.08 | 0.10 | 0.09 | 0.09 | 0.06 | 0.19 | 0.05 | 0.10 | 0.13 | 0.10 | 0.14 | 0.11 | 0.01 | 0.17 | 0.09 |
| Al$_2$O$_3$ | 21.11 | 21.19 | 21.12 | 20.68 | 20.26 | 20.72 | 20.79 | 20.29 | 20.53 | 20.16 | 20.28 | 20.39 | 20.48 | 20.62 | 20.47 | 20.20 | 20.31 |
| Cr$_2$O$_3$ | 0.02 | 0.02 | 0.01 | 0.01 | 0.01 | 0.03 | 0.00 | 0.01 | 0.02 | 0.01 | 0.00 | 0.00 | 0.01 | 0.01 | 0.06 | 0.07 | 0.00 |
| FeO | 35.77 | 27.40 | 31.08 | 30.49 | 26.09 | 31.22 | 30.04 | 29.71 | 32.78 | 30.99 | 30.71 | 32.56 | 32.19 | 30.19 | 31.72 | 27.31 | 30.69 |
| MnO | 1.48 | 7.71 | 3.84 | 4.92 | 10.08 | 4.15 | 0.84 | 2.08 | 1.04 | 2.30 | 2.22 | 1.25 | 1.75 | 0.87 | 5.92 | 8.28 | 5.58 |
| MgO | 3.45 | 1.50 | 2.09 | 1.74 | 0.82 | 1.99 | 2.75 | 2.20 | 1.67 | 1.19 | 1.30 | 1.59 | 2.05 | 2.97 | 2.28 | 1.41 | 2.15 |
| CaO | 1.95 | 5.74 | 5.30 | 4.76 | 5.09 | 3.60 | 7.67 | 8.43 | 7.11 | 7.62 | 7.89 | 6.77 | 6.51 | 7.32 | 2.25 | 5.92 | 3.76 |
| Total | 100.80 | 100.49 | 100.32 | 99.43 | 98.87 | 98.59 | 99.95 | 100.43 | 100.75 | 99.53 | 99.81 | 99.83 | 100.56 | 99.99 | 100.13 | 100.57 | 99.81 |
| Si | 2.95 | 2.95 | 2.95 | 2.98 | 2.99 | 3.01 | 3.01 | 2.99 | 3.00 | 3.01 | 3.01 | 3.00 | 2.99 | 3.02 | 3.03 | 2.99 | 3.01 |
| Ti | 0.00 | 0.01 | 0.00 | 0.01 | 0.01 | 0.01 | 0.00 | 0.01 | 0.00 | 0.01 | 0.01 | 0.01 | 0.01 | 0.01 | 0.00 | 0.01 | 0.01 |
| Al | 1.98 | 2.00 | 2.00 | 1.98 | 1.96 | 2.00 | 1.95 | 1.90 | 1.93 | 1.92 | 1.93 | 1.94 | 1.93 | 1.93 | 1.95 | 1.91 | 1.94 |
| Cr | 0.00 | 0.00 | 0.00 | 0.00 | 0.00 | 0.00 | 0.00 | 0.00 | 0.00 | 0.00 | 0.00 | 0.00 | 0.00 | 0.00 | 0.00 | 0.00 | 0.00 |
| Fe$^{3+}$ | 0.11 | 0.08 | 0.09 | 0.05 | 0.04 | 0.00 | 0.02 | 0.10 | 0.06 | 0.05 | 0.05 | 0.05 | 0.07 | 0.02 | 0.00 | 0.08 | 0.03 |
| Fe$^{2+}$ | 2.27 | 1.76 | 1.99 | 2.02 | 1.75 | 2.17 | 1.98 | 1.88 | 2.12 | 2.05 | 2.02 | 2.14 | 2.08 | 1.99 | 2.15 | 1.76 | 2.05 |
| Mn | 0.10 | 0.52 | 0.26 | 0.34 | 0.70 | 0.29 | 0.06 | 0.14 | 0.07 | 0.16 | 0.15 | 0.09 | 0.12 | 0.06 | 0.41 | 0.56 | 0.38 |
| Mg | 0.41 | 0.18 | 0.25 | 0.21 | 0.10 | 0.24 | 0.33 | 0.26 | 0.20 | 0.14 | 0.16 | 0.19 | 0.24 | 0.35 | 0.28 | 0.17 | 0.26 |
| Ca | 0.17 | 0.49 | 0.46 | 0.41 | 0.45 | 0.32 | 0.65 | 0.72 | 0.61 | 0.66 | 0.68 | 0.58 | 0.56 | 0.62 | 0.20 | 0.51 | 0.33 |
| Total | 8.00 | 8.00 | 8.00 | 8.00 | 8.00 | 8.03 | 8.00 | 8.00 | 8.00 | 8.00 | 8.00 | 8.00 | 8.00 | 8.00 | 8.01 | 8.00 | 8.00 |
| Alm | 77 | 60 | 67 | 68 | 58 | 72 | 66 | 63 | 71 | 68 | 67 | 71 | 69 | 66 | 71 | 59 | 68 |
| Sps | 3 | 18 | 9 | 11 | 23 | 10 | 2 | 5 | 2 | 5 | 5 | 3 | 4 | 2 | 13 | 19 | 13 |
| Grs | 6 | 17 | 15 | 14 | 15 | 10 | 22 | 24 | 20 | 22 | 23 | 19 | 19 | 21 | 6 | 17 | 11 |
| Pyr | 14 | 6 | 8 | 7 | 3 | 8 | 11 | 9 | 7 | 5 | 5 | 6 | 8 | 12 | 9 | 6 | 9 |
| X$_{Fe}$ | 0.85 | 0.91 | 0.89 | 0.91 | 0.95 | 0.90 | 0.86 | 0.88 | 0.91 | 0.93 | 0.93 | 0.92 | 0.89 | 0.85 | 0.89 | 0.91 | 0.89 |

**TABLE 3** Representative EMP analyses of chlorite, chloritoid, and epidote-zoisite grains in investigated micaschists (oxides in wt.%, cation in a pfu). $X_{Fe}$ = Fe/(Fe + Mg)

| Mineral | chlorite | chlorite | chlorite | chlorite | chloritoid | chloritoid | chloritoid | chloritoid |
|---|---|---|---|---|---|---|---|---|
| Sample | PK007 | PK007 | PK007 | PK007 | PK007 | PK007 | PK007 | PK007 |
| $SiO_2$ | 25.25 | 25.38 | 25.32 | 29.58 | 26.35 | 26.47 | 25.77 | 26.09 |
| $TiO_2$ | 0.11 | 0.10 | 0.09 | 0.05 | 0.00 | 0.00 | 0.00 | 0.00 |
| $Al_2O_3$ | 22.47 | 22.94 | 22.52 | 23.37 | 41.89 | 41.15 | 42.00 | 41.64 |
| $Cr_2O_3$ | 0.01 | 0.02 | 0.05 | 0.03 | 0.00 | 0.00 | 0.00 | 0.00 |
| FeO | 24.67 | 24.89 | 23.24 | 24.52 | 25.30 | 26.36 | 26.29 | 25.73 |
| MnO | 0.19 | 0.20 | 0.38 | 0.37 | 0.80 | 0.60 | 0.79 | 1.04 |
| MgO | 13.29 | 13.34 | 16.11 | 7.16 | 2.23 | 2.50 | 2.21 | 2.48 |
| CaO | 0.10 | 0.10 | 0.04 | 0.20 | 0.00 | 0.00 | 0.00 | 0.01 |
| $Na_2O$ | 0.00 | 0.00 | 0.01 | 0.03 | 0.35 | 0.00 | 0.01 | 0.02 |
| $K_2O$ | 0.05 | 0.01 | 0.02 | 0.88 | 0.26 | 0.00 | 0.00 | 0.11 |
| Total | 86.13 | 86.98 | 87.77 | 86.19 | 97.18 | 97.08 | 97.07 | 97.12 |
| Si | 5.39 | 5.36 | 5.27 | 6.21 | 2.07 | 2.09 | 2.04 | 2.06 |
| Ti | 0.02 | 0.02 | 0.01 | 0.01 | 0.00 | 0.00 | 0.00 | 0.00 |
| Al | 5.65 | 5.71 | 5.53 | 5.78 | 3.87 | 3.83 | 3.92 | 3.87 |
| Cr | 0.00 | 0.00 | 0.01 | 0.00 | 0.00 | 0.00 | 0.00 | 0.00 |
| $Fe^{2+}$ | 4.40 | 4.40 | 4.05 | 4.30 | 1.66 | 1.74 | 1.74 | 1.70 |
| Mn | 0.03 | 0.04 | 0.07 | 0.07 | 0.05 | 0.04 | 0.05 | 0.07 |
| Mg | 4.23 | 4.20 | 5.00 | 2.24 | 0.26 | 0.29 | 0.26 | 0.29 |
| Ca | 0.02 | 0.02 | 0.01 | 0.04 | 0.00 | 0.00 | 0.00 | 0.00 |
| Na | 0.00 | 0.00 | 0.01 | 0.03 | 0.11 | 0.00 | 0.00 | 0.01 |
| K | 0.03 | 0.00 | 0.01 | 0.47 | 0.05 | 0.00 | 0.00 | 0.02 |
| OH | 16.00 | 16.00 | 16.00 | 16.00 | 0.00 | 0.00 | 0.00 | 0.00 |
| Total | 35.78 | 35.76 | 35.96 | 35.14 | 8.08 | 8.00 | 8.01 | 8.02 |
| $X_{Fe}$ | 0.51 | 0.51 | 0.45 | 0.66 | 0.86 | 0.86 | 0.87 | 0.85 |

2. finding isopleths corresponding to the core composition of garnet grains and bulk rock composition; their interception is used as an input into the next step of calculations,

3. setting starting point for *P–T* path calculation (see point 2) outside of the garnet stability field but close to the garnet core isopleth intersection.

The calculations were performed using the Theriak-Domino software package (de Capitani & Petrakakis, 2010) with the Holland and Powell thermodynamic data set (1998 with updates to solution models through 2010), and appropriate mixing models in the system $SiO_2$–$TiO_2$–$Al_2O_3$–FeO–MgO–MnO–CaO–$Na_2O$–$K_2O$–$H_2O$ (KNCFMASHT). The solid solution models used in this study are white mica (Coggon & Holland, 2002), garnet and biotite (White et al., 2007), staurolite, chlorite and chloritoid (Holland & Powell, 1998), plagioclase (Holland & Powell, 2003), ilmenite (White, Powell, Holland, & Worley, 2000), and clinopyroxene (Green et al., 2007). Additionally, rutile and lawsonite were modelled as pure phases. Pure quartz and

$H_2O$ phases were added in excess to ensure their presence in all computations.

The first two analysis steps enabled us to characterize the stability field of garnet and the co-existing mineral assemblage at the onset of garnet growth. This allowed for validating the mineral assemblages observed in the samples and served as a test for the performance of the chosen set of solid solution models. For *P–T* path calculations, we chose garnet with the highest MnO content in the core, which were usually among the largest grains in the analysed population. The strategy relies on an assumption that the rock was not fractionated at the onset of garnet crystallization (Evans, 2004; Gaidies et al., 2006), and, therefore, the early-formed garnet grains should have the highest MnO content (e.g. George & Gaidies, 2017). Consequently, investigating such garnet grains allowed us to study in detail the whole history of the garnet growth including its earliest stages.

In sample PK028, garnet are up to 3 cm in diameter, and we were able to extract several grains from the rock matrix

| chloritoid PK007 | chloritoid PK007 | chloritoid PK007 | chloritoid PK007 | chloritoid PK007 | mineral sample | clinozoisite PK007 | clinozoisite PK028 | zoisite PK028 |
|---|---|---|---|---|---|---|---|---|
| 26.35 | 26.03 | 26.39 | 25.65 | 25.90 | $SiO_2$ | 38.65 | 37.30 | 37.70 |
| 0.00 | 0.08 | 0.00 | 0.06 | 0.07 | $TiO_2$ | 0.15 | 0.07 | 0.04 |
| 41.89 | 41.31 | 41.05 | 41.81 | 41.51 | $Al_2O_3$ | 30.34 | 24.53 | 25.14 |
| 0.00 | 0.00 | 0.00 | 0.00 | 0.00 | $Fe_2O_3$ | 5.69 | 10.50 | 11.95 |
| 25.29 | 26.30 | 26.27 | 25.88 | 26.02 | MnO | 0.39 | 0.12 | 0.10 |
| 0.80 | 0.79 | 0.60 | 0.90 | 1.31 | MgO | 0.05 | 0.08 | 0.07 |
| 2.23 | 2.23 | 2.48 | 2.59 | 1.96 | CaO | 23.96 | 21.20 | 21.78 |
| 0.00 | 0.06 | 0.01 | 0.11 | 0.21 | | | | |
| 0.35 | 0.24 | 0.24 | 0.09 | 0.06 | | | | |
| 0.26 | 0.03 | 0.06 | 0.03 | 0.06 | | | | |
| 97.17 | 97.07 | 97.10 | 97.12 | 97.10 | Total | 99.23 | 93.81 | 96.77 |
| 2.07 | 2.06 | 2.08 | 2.03 | 2.05 | $Si_4$ | 6.06 | 6.43 | 6.37 |
| 0.00 | 0.01 | 0.00 | 0.00 | 0.00 | $Ti_4$ | 0.02 | 0.01 | 0.01 |
| 3.88 | 3.85 | 3.82 | 3.89 | 3.88 | $Al_3$ | 5.61 | 4.99 | 5.01 |
| 0.00 | 0.00 | 0.00 | 0.00 | 0.00 | $Fe_3$ | 0.34 | 0.68 | 0.76 |
| 1.66 | 1.74 | 1.73 | 1.71 | 1.72 | $Mn_2$ | 0.05 | 0.02 | 0.01 |
| 0.05 | 0.05 | 0.04 | 0.06 | 0.09 | $Mg_2$ | 0.01 | 0.02 | 0.02 |
| 0.26 | 0.26 | 0.29 | 0.31 | 0.23 | Ca2 | 4.03 | 3.92 | 3.94 |
| 0.00 | 0.01 | 0.00 | 0.01 | 0.02 | | | | |
| 0.11 | 0.07 | 0.07 | 0.03 | 0.02 | | | | |
| 0.05 | 0.01 | 0.01 | 0.01 | 0.01 | | | | |
| 0.00 | 0.00 | 0.00 | 0.00 | 0.00 | | | | |
| 8.08 | 8.05 | 8.05 | 8.04 | 8.02 | Total | 16.12 | 16.07 | 16.12 |
| 0.86 | 0.87 | 0.86 | 0.85 | 0.88 | | | | |

and cut them approximately through their centre. In samples PK007 and PK033, the diameter of garnet grains is 2 mm at maximum, and we analysed their chemical composition in thin sections. Therefore, we might have not always analysed the true core of the garnet grains in these samples. However, these measurements produced P–T conditions close to the lower limit of the garnet stability field within 1% volume garnet growth contour for samples PK007 and PK033 and within 1 to 3% volume growth contours for sample PK028, which supported using them as representative for the onset of garnet growth.

In the third step, a Matlab script of Moynihan and Pattison (2013), which internally called the Theriak-Domino software (de Capitani & Petrakakis, 2010), searched the P–T space trying to find the closest match between the modelled and measured garnet compositions, using sample bulk compositions. The script required a starting point for calculations, which should be located outside the garnet stability field, as close as possible to the calculated P–T conditions at the onset of garnet growth (Moynihan & Pattison, 2013). The script

continually determined the effective matrix composition (e.g. Evans, 2004; Gaidies et al., 2008; Konrad-Schmolke et al., 2005), which was used in calculations for each step of garnet growth. The process was repeated for all data points along the inspected garnet profiles, from core to rim, resulting in reconstructed P–T paths. Classic geothermobaometric calculations were made using PTQuick software package (Simakov & Dolivo-Dobrovolsky, 2009).

Raman spectroscopy has been used to measure the wavenumber shift of quartz inclusions entrapped in garnet host. This work has been performed at two institutes. Sample PK028 was analysed with Raman spectrometer (DILOR LabRam with built-in Olympus BX 40 microscope) in the Institute of Geochemistry and Petrology, Eidgenössische Technische Hochschule Zürich (ETHZ), Switzerland. The grating was set to 1,800 grooves/mm, CCD sensor has a resolution of $1152 \times 298$ pixels (the focal length is ~40 cm which results in a spectral resolution of 1.3 $cm^{-1}$). The laser wavelength is 532.14 nm (max. 500 mW laser power at the source generated by a diode-pumped solid-state lasers). Direct measurements

**TABLE 4** Representative EMP analyses of white mica flakes in investigated micaschists (oxides in wt.%, cation in a pfu). bg - matrix, grt_inc - inclusions in garnet, ph - phengite, ms - muscovite, pg - paragonite, mg - margarite. $X_{Fe} = Fe/(Fe + Mg)$

| Sample | PK007b | PK007b | PK007b | PK007b | PK007b | PK007b | PK007b | PK007b | PK007b | PK007b | PK007b | PK028B | PK028B | PK028B | PK028B |
|---|---|---|---|---|---|---|---|---|---|---|---|---|---|---|---|
| Mineral | ph | Ph | ph | ph | ph | ms | ms | ms | ms | pg | pg | ph | ph | ph | ph |
| Point | bg | Bg | bg | bg | grt_inc | bg | bg | bg | bg | grt_inc | grt_inc | bg | bg | bg | grt_inc |
| $SiO_2$ | 51.41 | 51.82 | 51.97 | 51.33 | 51.40 | 45.75 | 45.75 | 46.26 | 46.66 | 46.43 | 48.82 | 51.27 | 51.97 | 50.76 | 49.94 |
| $TiO_2$ | 0.24 | 0.28 | 0.27 | 0.21 | 0.20 | 0.44 | 0.44 | 0.45 | 0.32 | 0.09 | 0.08 | 0.26 | 0.12 | 0.09 | 0.30 |
| $Al_2O_3$ | 28.99 | 28.69 | 30.29 | 30.41 | 27.66 | 36.83 | 36.83 | 36.16 | 35.43 | 38.83 | 39.25 | 27.38 | 27.12 | 26.41 | 27.25 |
| $Cr_2O_3$ | 0.03 | 0.01 | 0.01 | 0.03 | 0.01 | 0.00 | 0.00 | 0.02 | 0.04 | 0.02 | 0.02 | 0.04 | 0.00 | 0.01 | 0.02 |
| FeO | 2.34 | 2.57 | 1.73 | 1.87 | 3.06 | 1.10 | 1.10 | 0.99 | 1.36 | 0.70 | 0.24 | 2.67 | 2.46 | 3.40 | 4.11 |
| MnO | 0.08 | 0.00 | 0.00 | 0.00 | 0.02 | 0.07 | 0.07 | 0.06 | 0.02 | 0.04 | 0.02 | 0.03 | 0.00 | 0.06 | 0.04 |
| MgO | 2.29 | 2.68 | 2.17 | 1.95 | 2.47 | 0.40 | 0.40 | 0.61 | 0.92 | 0.06 | 0.04 | 2.92 | 3.28 | 3.12 | 2.43 |
| CaO | 0.04 | 0.00 | 0.00 | 0.05 | 0.10 | 0.02 | 0.02 | 0.00 | 0.00 | 0.46 | 0.21 | 0.01 | 0.05 | 0.04 | 0.00 |
| $Na_2O$ | 0.62 | 0.57 | 0.68 | 0.69 | 0.37 | 1.27 | 1.27 | 1.19 | 1.15 | 6.88 | 6.50 | 0.29 | 0.28 | 0.36 | 0.42 |
| $K_2O$ | 9.03 | 9.13 | 9.35 | 9.58 | 9.67 | 9.83 | 9.83 | 9.85 | 10.14 | 0.73 | 0.56 | 10.23 | 10.13 | 10.35 | 9.70 |
| $H_2O$ | 4.54 | 4.57 | 4.62 | 4.58 | 4.50 | 4.54 | 4.54 | 4.54 | 4.54 | 4.63 | 4.74 | 4.41 | 4.40 | 4.44 | 4.32 |
| Total | 99.61 | 100.32 | 101.09 | 100.70 | 99.46 | 100.25 | 100.25 | 100.13 | 100.58 | 98.87 | 100.48 | 99.51 | 99.81 | 99.04 | 98.53 |
| Si | 3.40 | 3.41 | 3.38 | 3.36 | 3.43 | 3.05 | 3.02 | 3.06 | 3.08 | 3.00 | 3.08 | 3.43 | 3.46 | 3.43 | 3.39 |
| Ti | 0.01 | 0.01 | 0.01 | 0.01 | 0.01 | 0.02 | 0.02 | 0.02 | 0.02 | 0.00 | 0.00 | 0.01 | 0.01 | 0.01 | 0.02 |
| Al | 2.26 | 2.22 | 2.32 | 2.35 | 2.17 | 2.85 | 2.87 | 2.82 | 2.76 | 2.96 | 2.92 | 2.16 | 2.13 | 2.10 | 2.18 |
| Cr | 0.00 | 0.00 | 0.00 | 0.00 | 0.00 | 0.00 | 0.00 | 0.00 | 0.00 | 0.00 | 0.00 | 0.00 | 0.00 | 0.00 | 0.00 |
| $Fe^{2+}$ | 0.13 | 0.14 | 0.09 | 0.10 | 0.17 | 0.06 | 0.06 | 0.06 | 0.08 | 0.04 | 0.01 | 0.15 | 0.14 | 0.19 | 0.23 |
| Mn | 0.00 | 0.00 | 0.00 | 0.00 | 0.00 | 0.00 | 0.00 | 0.00 | 0.00 | 0.00 | 0.00 | 0.00 | 0.00 | 0.00 | 0.00 |
| Mg | 0.23 | 0.26 | 0.21 | 0.19 | 0.25 | 0.05 | 0.04 | 0.06 | 0.09 | 0.01 | 0.00 | 0.29 | 0.33 | 0.31 | 0.25 |
| Ca | 0.00 | 0.00 | 0.00 | 0.00 | 0.01 | 0.00 | 0.00 | 0.00 | 0.00 | 0.03 | 0.01 | 0.00 | 0.00 | 0.00 | 0.00 |
| Na | 0.08 | 0.07 | 0.09 | 0.09 | 0.05 | 0.17 | 0.16 | 0.15 | 0.15 | 0.86 | 0.80 | 0.04 | 0.04 | 0.05 | 0.06 |
| K | 0.76 | 0.77 | 0.78 | 0.80 | 0.82 | 0.82 | 0.83 | 0.83 | 0.85 | 0.06 | 0.05 | 0.87 | 0.86 | 0.89 | 0.84 |
| H | 2.00 | 2.00 | 2.00 | 2.00 | 2.00 | 2.00 | 2.00 | 2.00 | 2.00 | 2.00 | 2.00 | 1.97 | 1.95 | 2.00 | 1.96 |
| Total | 8.88 | 8.89 | 8.89 | 8.90 | 8.91 | 9.01 | 9.01 | 9.00 | 9.03 | 8.97 | 8.88 | 8.92 | 8.90 | 8.99 | 8.93 |
| $X_{Fe}$ | 0.37 | 0.35 | 0.31 | 0.35 | 0.41 | 0.54 | 0.61 | 0.48 | 0.45 | 0.86 | 0.75 | 0.34 | 0.30 | 0.38 | 0.49 |
| Ms | 90 | 92 | 90 | 89 | 94 | 83 | 84 | 85 | 85 | 6 | 5 | 96 | 95 | 94 | 93 |
| Pg | 9 | 8 | 10 | 10 | 6 | 17 | 16 | 15 | 15 | 90 | 93 | 4 | 4 | 5 | 7 |
| Mg | 0 | 0 | 0 | 0 | 1 | 0 | 0 | 0 | 0 | 3 | 2 | 0 | 0 | 0 | 0 |

of laser power were performed with a coherent LaserCheck hand-held device. The output laser power was measured to be 19.7 mW under 100× objective after the application of laser filters. All three samples PK028, PK033, and PK007 were analysed with Raman spectroscopy (Qontor Raman spectrometer, Renishaw) at Institute of Geological Sciences, University of Wrocław, Poland. The grating was set to 1,200 grooves/mm, CCD sensor has a resolution of 1024 × 256 pixels, and the spectral resolution is 1.3 cm$^{-1}$. The laser wavelength is 785 nm. The laser source energy is 100 mW and we used less than 25% of the input energy to reduce heating effect. Considering the amount of energy lost through the optic system, the energy reaching the thin-section surface should be less than ~20 mW. An unstrained gem-quality quartz crystal was used as standard. The PK028 was measured in the two different laboratories for comparison

purposes, and although we did not measure exactly the same quartz inclusions, similar statistical distributions (max and mean) of the Raman shifts were achieved.

# 4 | PETROGRAPHY AND MINERAL CHEMISTRY

## 4.1 | Sample PK007

The micaschist sample PK007 displays millimetre-sized garnet porphyroblasts in a schistose matrix mainly consisting of quartz, K-white mica (muscovite, phengite), biotite, and chlorite. Accessory minerals are paragonite, margarite, rutile, ilmenite, zircon, and apatite.

| PK028B | PK028B | PK028B | PK028B | PK028B | PK028B | PK028B | PK028B | PK028B | PK028B | PK033 | PK033 | PK033 | PK033 | PK033 | PK033 |
|---|---|---|---|---|---|---|---|---|---|---|---|---|---|---|---|
| ms | ms | ms | ms | ms | ms | pg | pg | pg | pg | ms | ms | ms | ms | ph | ph |
| grt_inc | grt_inc | grt_inc | bg | bg | bg | grt_inc_pg | grt_inc_pg | grt_inc_pg | grt_inc_pg | bg | bg | bg | bg | bg | bg |
| 50.48 | 47.84 | 47.75 | 48.06 | 46.09 | 47.05 | 47.36 | 48.08 | 48.06 | 47.73 | 47.38 | 47.38 | 46.27 | 46.76 | 48.98 | 50.21 |
| 0.26 | 0.58 | 0.31 | 0.01 | 0.26 | 0.00 | 0.08 | 0.08 | 0.14 | 0.07 | 0.42 | 0.39 | 0.14 | 0.45 | 0.31 | 0.35 |
| 29.22 | 32.49 | 32.46 | 33.50 | 35.99 | 34.43 | 39.65 | 39.85 | 39.22 | 38.76 | 34.03 | 34.16 | 36.80 | 36.52 | 30.68 | 30.24 |
| 0.00 | 0.02 | 0.01 | 0.00 | 0.00 | 0.00 | 0.02 | 0.02 | 0.02 | 0.02 | 0.12 | 0.04 | 0.30 | 0.10 | 0.00 | 0.16 |
| 3.80 | 3.13 | 2.85 | 1.68 | 1.47 | 1.75 | 0.69 | 0.72 | 0.73 | 1.28 | 1.88 | 1.28 | 0.87 | 0.93 | 1.74 | 1.57 |
| 0.00 | 0.00 | 0.00 | 0.10 | 0.06 | 0.05 | 0.03 | 0.04 | 0.00 | 0.02 | 0.03 | 0.00 | 0.00 | 0.00 | 0.00 | 0.03 |
| 2.07 | 1.21 | 1.14 | 1.16 | 0.56 | 0.79 | 0.06 | 0.12 | 0.07 | 0.17 | 1.38 | 1.05 | 0.42 | 0.46 | 1.89 | 2.15 |
| 0.00 | 0.04 | 0.00 | 0.00 | 0.00 | 0.00 | 0.14 | 0.15 | 0.22 | 0.12 | 0.00 | 0.01 | 0.02 | 0.00 | 0.03 | 0.00 |
| 0.36 | 1.00 | 0.81 | 0.14 | 0.34 | 0.17 | 6.17 | 6.64 | 6.77 | 7.70 | 0.63 | 0.57 | 1.20 | 1.20 | 0.61 | 0.56 |
| 9.99 | 9.40 | 9.78 | 10.75 | 10.88 | 11.13 | 1.48 | 0.72 | 1.32 | 0.53 | 9.95 | 10.06 | 9.33 | 9.44 | 9.81 | 9.82 |
| 4.36 | 4.42 | 4.42 | 4.45 | 4.41 | 4.36 | 4.69 | 4.66 | 4.74 | 4.73 | 4.54 | 4.51 | 4.54 | 4.57 | 4.47 | 4.53 |
| 100.54 | 100.13 | 99.53 | 99.85 | 100.06 | 99.73 | 100.37 | 101.08 | 101.29 | 101.13 | 100.36 | 99.45 | 99.89 | 100.43 | 98.52 | 99.62 |
| 3.36 | 3.19 | 3.20 | 3.20 | 3.07 | 3.15 | 3.02 | 3.03 | 3.04 | 3.03 | 3.13 | 3.15 | 3.05 | 3.07 | 3.29 | 3.33 |
| 0.01 | 0.03 | 0.02 | 0.00 | 0.01 | 0.00 | 0.00 | 0.00 | 0.01 | 0.00 | 0.02 | 0.02 | 0.01 | 0.02 | 0.02 | 0.02 |
| 2.29 | 2.55 | 2.56 | 2.63 | 2.82 | 2.71 | 2.98 | 2.96 | 2.92 | 2.90 | 2.65 | 2.68 | 2.86 | 2.83 | 2.43 | 2.36 |
| 0.00 | 0.00 | 0.00 | 0.00 | 0.00 | 0.00 | 0.00 | 0.00 | 0.00 | 0.00 | 0.01 | 0.00 | 0.02 | 0.01 | 0.00 | 0.01 |
| 0.21 | 0.17 | 0.16 | 0.09 | 0.08 | 0.10 | 0.04 | 0.04 | 0.04 | 0.07 | 0.10 | 0.07 | 0.05 | 0.05 | 0.10 | 0.09 |
| 0.00 | 0.00 | 0.00 | 0.01 | 0.00 | 0.00 | 0.00 | 0.00 | 0.00 | 0.00 | 0.00 | 0.00 | 0.00 | 0.00 | 0.00 | 0.00 |
| 0.21 | 0.12 | 0.11 | 0.12 | 0.06 | 0.08 | 0.01 | 0.01 | 0.01 | 0.02 | 0.14 | 0.10 | 0.04 | 0.05 | 0.19 | 0.21 |
| 0.00 | 0.00 | 0.00 | 0.00 | 0.00 | 0.00 | 0.01 | 0.01 | 0.02 | 0.01 | 0.00 | 0.00 | 0.00 | 0.00 | 0.00 | 0.00 |
| 0.05 | 0.13 | 0.11 | 0.02 | 0.04 | 0.02 | 0.76 | 0.81 | 0.83 | 0.95 | 0.08 | 0.07 | 0.15 | 0.15 | 0.08 | 0.07 |
| 0.85 | 0.80 | 0.84 | 0.91 | 0.92 | 0.95 | 0.12 | 0.06 | 0.11 | 0.04 | 0.84 | 0.85 | 0.79 | 0.79 | 0.84 | 0.83 |
| 1.93 | 1.96 | 1.98 | 1.97 | 1.96 | 1.95 | 1.99 | 1.96 | 2.00 | 2.00 | 2.00 | 2.00 | 2.00 | 2.00 | 2.00 | 2.00 |
| 8.90 | 8.96 | 8.97 | 8.94 | 8.97 | 8.95 | 8.93 | 8.89 | 8.96 | 9.02 | 8.98 | 8.95 | 8.97 | 8.96 | 8.94 | 8.92 |
| 0.51 | 0.59 | 0.58 | 0.45 | 0.59 | 0.55 | 0.86 | 0.78 | 0.87 | 0.81 | 0.43 | 0.41 | 0.54 | 0.53 | 0.34 | 0.29 |
| 94 | 86 | 88 | 98 | 96 | 98 | 13 | 7 | 11 | 4 | 91 | 92 | 84 | 84 | 91 | 92 |
| 6 | 14 | 12 | 2 | 4 | 2 | 85 | 92 | 87 | 95 | 9 | 8 | 16 | 16 | 9 | 8 |
| 0 | 0 | 0 | 0 | 0 | 0 | 1 | 1 | 2 | 1 | 0 | 0 | 0 | 0 | 0 | 0 |

In the rock matrix, millimetre-thick, strongly elongated quartz lenses alternate with laminae composed of muscovite, rare biotite, and chlorite. However, refolded quartz lenses and white mica plates oblique to the penetrative foliation are also preserved throughout the sample, giving rise to two sets of foliations (S1 and S2, Figure 2a and b). Similarly two foliations may also be preserved in garnet porphyroblasts (Figure 2c). Therefore, we interpret the domains exhibiting the folded foliation S1 as microlithons, while the penetrative, younger foliation S2 represents cleavage domains. We suggest that the S2 foliation was reactivated forming a complex planar structure (S2+3), which is indicative of non-coaxial ductile deformation postdating folding. This conclusion is confirmed by occurrences of kinematic indicators, including S-C type structures and asymmetric sigma-type pressure shadows around plagioclase and garnet porphyroblasts, that can be observed in rock sections cut parallel to mineral lineation and perpendicular to the S2+3 planes.

Subhedral garnet porphyroblasts range from 0.2 up to 2 mm in size, and they commonly contain polymineralic inclusions comprising chloritoid, K-white mica and paragonite (Figure 3a) as well as margarite, clinozoisite, and quartz (Figure 3b and c). We interpret the latter type of polymineralic inclusions potentially as pseudomorphs after lawsonite that could have been produced according to the following mineral reaction (Chatterjee, 1976; Gomez-Pugnaire et al., 1985):

$$5Lws = 2Czo + Mrg + 2Qz + 8H_2O.$$

**TABLE 5** Representative EMP analyses of plagioclase grains in investigated micaschists (oxides in wt.%, cation in a pfu)

| Sample | PK007 | PK007 | PK007 | PK007 | PK007 | PK007 | PK007 | PK007 | PK007 | PK028 |
|---|---|---|---|---|---|---|---|---|---|---|
| $SiO_2$ | 62.53 | 64.50 | 65.81 | 63.34 | 62.72 | 63.23 | 62.77 | 68.61 | 68.12 | 74.53 |
| $TiO_2$ | 0.00 | 0.00 | 0.00 | 0.00 | 0.00 | 0.00 | 0.00 | 0.00 | 0.00 | 0.00 |
| $Al_2O_3$ | 23.07 | 21.76 | 20.83 | 23.34 | 23.24 | 22.97 | 23.72 | 19.26 | 19.30 | 15.79 |
| FeO | 0.80 | 0.17 | 0.17 | 0.15 | 0.20 | 0.06 | 0.00 | 0.04 | 0.20 | 0.62 |
| CaO | 4.18 | 2.36 | 1.74 | 4.40 | 4.23 | 3.85 | 4.75 | 0.11 | 0.10 | 1.62 |
| $Na_2O$ | 10.07 | 11.26 | 10.91 | 9.58 | 9.73 | 9.79 | 9.54 | 11.62 | 11.41 | 7.82 |
| $K_2O$ | 0.03 | 0.10 | 0.05 | 0.07 | 0.07 | 0.09 | 0.05 | 0.03 | 0.06 | 0.04 |
| Total | 100.68 | 100.15 | 99.51 | 100.88 | 100.19 | 99.99 | 100.83 | 99.67 | 99.19 | 100.42 |
| Si | 2.77 | 2.85 | 2.91 | 2.78 | 2.78 | 2.80 | 2.76 | 3.01 | 3.00 | 3.19 |
| Ti | 0.00 | 0.00 | 0.00 | 0.00 | 0.00 | 0.00 | 0.00 | 0.00 | 0.00 | 0.00 |
| Al | 1.20 | 1.13 | 1.09 | 1.21 | 1.21 | 1.20 | 1.23 | 0.99 | 1.00 | 0.80 |
| $Fe^{2+}$ | 0.03 | 0.01 | 0.01 | 0.01 | 0.01 | 0.00 | 0.00 | 0.00 | 0.01 | 0.02 |
| Ca | 0.20 | 0.11 | 0.08 | 0.21 | 0.20 | 0.18 | 0.22 | 0.01 | 0.01 | 0.07 |
| Na | 0.86 | 0.96 | 0.94 | 0.82 | 0.84 | 0.84 | 0.81 | 0.99 | 0.97 | 0.65 |
| K | 0.00 | 0.01 | 0.00 | 0.00 | 0.00 | 0.01 | 0.00 | 0.00 | 0.00 | 0.00 |
| Total | 5.06 | 5.07 | 5.02 | 5.02 | 5.04 | 5.03 | 5.03 | 4.99 | 4.99 | 4.74 |
| Ab | 81 | 89 | 92 | 79 | 80 | 82 | 78 | 99 | 99 | 90 |
| An | 19 | 10 | 8 | 20 | 19 | 18 | 22 | 1 | 1 | 10 |
| Or | 0 | 1 | 0 | 0 | 0 | 0 | 0 | 0 | 0 | 0 |

Garnet grains in the PK007 sample typically exhibit complex chemical zonation (Figures 4a, 5a-c and Table 2), with bell-shaped spessartine profile in their core ($X_{sps}$ decreasing from ~23 to ~10), sharp spessartine increase in the inner rim ($X_{sps}$ ~15), followed by a decrease towards the outer rim ($X_{sps}$ ~9). The variation in spessartine content is coupled with a gradual core-to-rim increase in almandine content ($X_{alm}$ from ~57 to ~72). Grossular concentration displays relatively low value in the inner core ($X_{grs}$ ~12.5 to ~17.5), which increases outwards in the most part of the outer core and rim ($X_{grs}$ from ~18 to ~20). However, the grossular concentration decreases rapidly at the interface between outer core and inner rim, as well as in outer rim ($X_{grs}$ ~14 and ~10, respectively, Figure 4a). We interpret the described chemical zonation as having formed in response to two distinct stages of garnet growth. We use Grt1 to denote the garnet forming the internal parts of garnet grains, and Grt2 for garnet rims. Interestingly, Grt1 entraps rutile inclusions, while Grt2 contains mostly ilmenite inclusions, indicating that these garnet types were equilibrated under different *P–T* conditions (Figures S1 and S2). This conclusion is also confirmed by the occurrence of polymineral clinozoisite, margarite, and quartz inclusions within Grt1, which we have interpreted as presumed pseudomorphs after lawsonite (Figure 3b and c). Furthermore, chloritoid inclusions form blasts with grain size of up to 100 microns (Figure 3a), showing quite uniform chemical composition characterized by X(cld) = Fe/(Mg + Fe) ranging from 0.79 to 0.88 (Table 3). Additionally, rare

chlorite inclusions were documented in both Grt1 and Grt2 (Table 3).

K-white mica may be divided into highly abundant low $Si^{4+}$ grains for which $Si^{4+}$ content ranges from 3.0 to 3.20 p.f.u. and a less common set displaying phengitic composition with $Si^{4+}$ content ranging from 3.25 to 3.45 p.f.u. (Figure 6, Table 4). The phengitic white mica were documented in rock matrix, mostly in the microlithons, but also in the cleavage domains, and as inclusions in the core parts of garnet grains (Grt1). Low $Si^{4+}$ K-white mica grains occur abundantly in the matrix of the investigated sample, often within the cleavage domains, and they are also preserved as inclusions in the Grt2.

Plagioclase occurs in the matrix, generally forming small grains reaching up to 0.03 mm in diameter as well as porphyroblasts with diameter of up to 0.5 mm. Small matrix grains display an oligoclase composition, with maximum 22 mol% of $X_{An}$ (Table 5), and porphyroblasts show albitic cores, with oligoclase rims, which are well developed in the pressure shadows.

Small biotite flakes were documented as inclusions in Grt2 as well as matrix grains in the PK007 micaschist sample. Biotite is characterized by $X_{Mg}$ varying from 0.29 to 0.52 (Table 6).

Based on textural observations, we distinguish two mineral assemblages in PK007: the M1 assemblage represented by Grt1 and Cld + Ph + Pg + [Lws] + Chl +Rt + Qz predominantly forming inclusions in Grt1. Mineral phases reported in

| PK028 | PK028 | PK028 | PK028 | PK028 | PK033 | PK033 | PK033 | PK033 | PK033 |
|---|---|---|---|---|---|---|---|---|---|
| 60.55 | 63.34 | 62.58 | 65.20 | 67.75 | 62.26 | 60.23 | 63.67 | 64.55 | 68.75 |
| 0.00 | 0.00 | 0.00 | 0.00 | 0.00 | 0.00 | 0.00 | 0.00 | 0.00 | 0.00 |
| 24.15 | 23.09 | 23.46 | 22.02 | 20.64 | 24.00 | 25.09 | 22.74 | 22.28 | 19.52 |
| 0.06 | 0.07 | 0.07 | 0.09 | 0.13 | 0.28 | 0.09 | 0.15 | 0.03 | 0.17 |
| 5.74 | 4.37 | 5.08 | 3.06 | 1.27 | 5.44 | 6.76 | 3.84 | 3.43 | 0.14 |
| 8.05 | 9.01 | 8.61 | 9.92 | 10.59 | 8.46 | 7.66 | 9.56 | 9.69 | 11.57 |
| 0.13 | 0.15 | 0.18 | 0.09 | 0.20 | 0.06 | 0.08 | 0.07 | 0.07 | 0.05 |
| 98.68 | 100.03 | 99.98 | 100.38 | 100.58 | 100.50 | 99.91 | 100.03 | 100.05 | 100.20 |
| 2.72 | 2.80 | 2.77 | 2.86 | 2.95 | 2.75 | 2.68 | 2.81 | 2.84 | 3.00 |
| 0.00 | 0.00 | 0.00 | 0.00 | 0.00 | 0.00 | 0.00 | 0.00 | 0.00 | 0.00 |
| 1.28 | 1.20 | 1.23 | 1.14 | 1.06 | 1.25 | 1.32 | 1.18 | 1.16 | 1.00 |
| 0.00 | 0.00 | 0.00 | 0.00 | 0.00 | 0.01 | 0.01 | 0.00 | 0.01 | 0.01 |
| 0.28 | 0.21 | 0.24 | 0.14 | 0.06 | 0.26 | 0.32 | 0.18 | 0.16 | 0.01 |
| 0.70 | 0.77 | 0.74 | 0.84 | 0.89 | 0.72 | 0.66 | 0.82 | 0.83 | 0.98 |
| 0.01 | 0.01 | 0.01 | 0.01 | 0.01 | 0.00 | 0.01 | 0.00 | 0.00 | 0.00 |
| 4.99 | 4.99 | 4.99 | 5.00 | 4.97 | 4.99 | 4.99 | 5.01 | 4.99 | 4.99 |
| 71 | 78 | 75 | 85 | 93 | 74 | 67 | 81 | 83 | 99 |
| 28 | 21 | 24 | 15 | 6 | 26 | 33 | 18 | 16 | 1 |
| 1 | 1 | 1 | 1 | 1 | 0 | 1 | 0 | 0 | 0 |

square brackets represent presumed pseudomorphs. Phengitic white mica, chlorite, and rutile are also present in the matrix of the inspected sample. The M2 assemblage represented by Grt2 and Ms + Bt + Pl+ Chl +Ilm + Qz is observed in the rims of Grt2 grains as well as in the matrix.

## 4.2 | SAMPLE PK028

The micaschist sample PK028 consists of garnet porphyroblasts in a schistose matrix mainly composed of quartz, K-white mica, biotite, and plagioclase. Accessory minerals are paragonite, rutile, ilmenite, epidote, zircon, and apatite.

The rock matrix displays quartz lenses and laminae that alternate with muscovite-dominated laminae. White mica plates oriented obliquely to the penetrative foliation are rarely preserved in the quartz-rich laminae. Therefore, we interpret the quartz-rich domains as microlithons with preserved older foliation (S1), while the muscovite rich as penetrative and younger cleavage domains (S2). In contrast to sample PK007, only S1 foliation is preserved within garnet porphyroblasts (Figure 2d).

The inspected garnet, reaching 3 cm in diameter, display a weakly developed bell-shaped spessartine profile in the inner part (decrease in $X_{Sps}$ from ~5 to ~1), followed by its gradual increase within the inner rim ($X_{Sps}$ to ~5), and a relatively sharp drop towards the outer rim ($X_{Sps}$ to ~1, Figures 4b, 5d-f and Table 2). Grossular content roughly mimics the spessartine concentration, exhibiting the highest concentration in the inner core ($X_{Grs}$ = 24), gradually dropping towards the outer core ($X_{Grs}$ to ~15), and showing a sharp increase in the inner rim ($X_{Grs}$ to ~25), and a decrease towards the outer rim ($X_{Grs}$ to 18). A generally stable pyrope content is observed in the core parts ($X_{Prp}$ ~5–7) and it gradually increases towards the rim ($X_{Prp}$ to ~10). Almandine is characterized by a fairly stable concentration in the inner core ($X_{Alm}$ ~68), which increases towards the outer core ($X_{Alm}$ to ~78), decreases towards the inner rim ($X_{Alm}$ to ~62) and again increases towards the outer rim ($X_{Alm}$ ~68). Furthermore, compositional maps reveal that garnet rims display oscillatory zoning, which is particularly well pronounced for grossular and slightly less prominent for the spessartine component (Figure 5d and e). The grossular and spessartine oscillatory zoning patterns are euhedral and parallel to crystal faces pointing to the observed zoning being a growth feature. Interestingly, garnet in PK028 sample commonly contain rutile and ilmenite inclusions that are typically in contact. However, a close inspection of their textural position shows that ilmenite fills cracks in garnet grains and in some cases also replaces rutile needles that are cut by cracks (Figure 2e). It suggests that ilmenite post-dates rutile and is either a product of retrogression or a fluid-mediated phase introduced to garnet after its crystallization. These two alternative scenarios could not be resolved based solely on the inspection of *SEM* images. However, we ruled out the possibility

**TABLE 6** Representative EMP analyses of dark mica flakes in investigated micaschists (oxides in wt.%, cation in a pfu). $X_{Fe} = Fe/(Fe + Mg)$

| Sample | PK007 | PK007 | PK007 | PK007 | PK007 | PK028B | PK028B | PK028B | PK028B | PK028B | PK033 | PK033 |
|---|---|---|---|---|---|---|---|---|---|---|---|---|
| $SiO_2$ | 35.18 | 35.2 | 35.67 | 35.71 | 35.46 | 37.81 | 36.95 | 37.45 | 36.43 | 35.21 | 35.5 | 35.76 |
| $TiO_2$ | 1.42 | 1.74 | 1.64 | 2.26 | 2.4 | 1.18 | 1.17 | 1.23 | 2.95 | 2.67 | 2.53 | 2.52 |
| $Al_2O_3$ | 18.12 | 18.61 | 19.36 | 19 | 19.15 | 19.86 | 19.62 | 19.74 | 17.89 | 18.54 | 18.9 | 18.47 |
| $Cr_2O_3$ | 0.01 | 0.05 | 0.04 | 0.05 | 0.01 | 0 | 0 | 0.15 | 0.05 | 0.02 | 0.03 | 0 |
| FeO | 20.73 | 21.18 | 20.47 | 20.59 | 20.75 | 17.04 | 16.55 | 16.36 | 18.73 | 19.47 | 19.28 | 19.9 |
| MnO | 0.08 | 0.07 | 0.18 | 0.04 | 0.04 | 0.11 | 0.1 | 0.15 | 0.16 | 0.09 | 0.29 | 0.12 |
| MgO | 9.03 | 8.51 | 8.62 | 8.18 | 7.79 | 11.32 | 10.87 | 11.06 | 9.93 | 9.66 | 8.86 | 8.42 |
| CaO | 0.04 | 0.02 | 0 | 0.04 | 0.05 | 0.07 | 0.02 | 0.01 | 0.03 | 0.05 | 0 | 0.04 |
| $Na_2O$ | 0.01 | 0.05 | 0.16 | 0.06 | 0.04 | 0.03 | 0.06 | 0.02 | 0.05 | 0.05 | 0.17 | 0.04 |
| $K_2O$ | 9.03 | 9.38 | 9.31 | 9.21 | 9.34 | 9.45 | 9.65 | 9.7 | 9.42 | 9.55 | 9.21 | 9.14 |
| $H_2O$ | 3.85 | 3.88 | 3.93 | 3.92 | 3.94 | 4.08 | 4 | 4.04 | 3.97 | 3.93 | 3.92 | 3.9 |
| Total | 97.5 | 98.69 | 99.38 | 99.06 | 98.97 | 100.95 | 98.99 | 99.91 | 99.61 | 99.24 | 98.69 | 98.31 |
| Si | 2.78 | 2.77 | 2.78 | 2.80 | 2.79 | 2.84 | 2.84 | 2.85 | 2.82 | 2.74 | 2.78 | 2.82 |
| Ti | 0.09 | 0.10 | 0.10 | 0.13 | 0.14 | 0.07 | 0.07 | 0.07 | 0.17 | 0.16 | 0.15 | 0.15 |
| Al | 1.69 | 1.73 | 1.78 | 1.76 | 1.78 | 1.76 | 1.78 | 1.77 | 1.63 | 1.70 | 1.75 | 1.72 |
| Cr | 0.00 | 0.00 | 0.00 | 0.00 | 0.00 | 0.00 | 0.00 | 0.01 | 0.00 | 0.00 | 0.00 | 0.00 |
| $Fe^{2+}$ | 1.37 | 1.39 | 1.33 | 1.35 | 1.37 | 1.07 | 1.06 | 1.04 | 1.21 | 1.27 | 1.26 | 1.31 |
| Mn | 0.01 | 0.01 | 0.01 | 0.00 | 0.00 | 0.01 | 0.01 | 0.01 | 0.01 | 0.01 | 0.02 | 0.01 |
| Mg | 1.07 | 1.00 | 1.00 | 0.96 | 0.92 | 1.27 | 1.25 | 1.25 | 1.15 | 1.12 | 1.04 | 0.99 |
| Ca | 0.00 | 0.00 | 0.00 | 0.00 | 0.00 | 0.01 | 0.00 | 0.00 | 0.00 | 0.00 | 0.00 | 0.00 |
| Na | 0.00 | 0.01 | 0.02 | 0.01 | 0.01 | 0.00 | 0.01 | 0.00 | 0.01 | 0.01 | 0.03 | 0.01 |
| K | 0.91 | 0.94 | 0.93 | 0.92 | 0.94 | 0.90 | 0.95 | 0.94 | 0.93 | 0.95 | 0.92 | 0.92 |
| H | 3.67 | 3.66 | 3.67 | 3.67 | 3.69 | 3.66 | 3.67 | 3.67 | 3.67 | 3.67 | 3.67 | 3.67 |
| Total | 7.92 | 17.96 | 17.93 | 17.85 | 17.87 | 17.87 | 17.90 | 17.87 | 17.86 | 17.96 | 17.88 | 17.82 |
| $X_{Fe}$ | 0.56 | 0.58 | 0.57 | 0.58 | 0.60 | 0.46 | 0.46 | 0.45 | 0.51 | 0.53 | 0.55 | 0.57 |

that ilmenite could be produced at the expense of garnet as there is no change of garnet chemical composition around ilmenite inclusions.

White mica flakes show a wide range of $Si^{4+}$ content from 3.01 to 3.40 cations p.f.u. (Figure 6), while $Na^+$ varies from 0.10 to 0.90 cations p.f.u. (Table 4). Paragonite occurs mostly as inclusions in garnet grains (Figure 5f) and exhibits Na/(Na + K) ratio between 0.84 and 0.95 (Table 4). Phengitic mica are preserved both in the matrix and as inclusions in garnet grains. The phengitic mica in the matrix are usually parallel to the older foliation planes (S1), but they are also found within cleavage domains (S2). They are characterized by $Si^{4+}$ content ranging from 3.25 to 3.40 cations p.f.u. White mica with low $Si^{4+}$ content occur mostly in the matrix ranging in $Si^{4+}$ content from 3.01 to 3.22 cations p.f.u. We suggest that the nearly continuous composition range of white mica from muscovite to phengite observed in this sample might have resulted from $Si^{4+}$ modification owing to, for example, dissolution-transport-precipitation, similarly to metapelites from the Longmen Shan in China (Airaghi et al., 2017).

Plagioclase either forms inclusions in garnet or occurs as matrix grains reaching up to 0.04 mm in diameter. Plagioclase grains in PK028 sample exhibit chemical compositions from albite ($X_{Ab} = 6$) in the core to oligoclase ($X_{Ab} = 28$, Table 5) in the rims. Zoisite inclusions were documented within garnet grains with a size reaching up to 5–10 microns, mostly in association with quartz and paragonite (Figure 3d).

Based on textural setting, we distinguish two mineral assemblages in this micaschist sample. The M1 assemblage represented by Grt and Ph + Pg + Rt + Qz in garnet grains, and the M2 assemblage comprising Ms + Bt + Pl+ Ilm + Qz and observed in the matrix of the investigated micaschist.

## 4.3 | Sample PK033

Sample PK033 is a micaschist composed of garnet, muscovite, biotite, staurolite, plagioclase, quartz, and accessory ilmenite, apatite, tourmaline, and secondary chlorites. In contrast to samples PK007 and PK028, the inspected micaschist PK033 is characterized by a single set of planar

**TABLE 7** Representative EMP analyses of ilmenite grains in investigated micaschists (oxides in wt.%, cation in a pfu)

| Sample | PK007 | PK007 | PK007 | PK007 | PK028 | PK028 | PK028 | PK033 |
|---|---|---|---|---|---|---|---|---|
| Point | grt_inc | grt_inc | bg | bg | grt_inc | grt_inc | bg | bg |
| $SiO_2$ | 0.28 | 0.04 | 0.03 | 0.03 | 0.02 | 0.00 | 0.02 | 2.14 |
| $TiO_2$ | 51.54 | 51.64 | 53.49 | 53.52 | 47.20 | 52.59 | 51.80 | 49.67 |
| $Al_2O_3$ | 0.00 | 0.00 | 0.02 | 0.00 | 0.00 | 0.04 | 0.00 | 1.47 |
| FeO | 45.05 | 45.37 | 41.72 | 42.51 | 45.50 | 44.49 | 32.78 | 44.23 |
| MnO | 1.96 | 2.16 | 3.02 | 3.53 | 1.67 | 1.26 | 11.21 | 2.82 |
| MgO | 0.05 | 0.03 | 0.04 | 0.02 | 0.01 | 0.00 | 0.09 | 0.15 |
| CaO | 0.14 | 0.14 | 0.00 | 0.00 | 0.10 | 0.00 | 0.02 | 0.71 |
| Total | 99.03 | 99.38 | 98.33 | 99.60 | 94.51 | 98.38 | 95.92 | 101.19 |
| Si | 0.01 | 0.00 | 0.00 | 0.00 | 0.00 | 0.00 | 0.00 | 0.05 |
| Ti | 0.99 | 0.99 | 1.03 | 1.02 | 0.95 | 1.02 | 1.03 | 0.92 |
| Al | 0.00 | 0.00 | 0.00 | 0.00 | 0.00 | 0.00 | 0.00 | 0.04 |
| $Fe^2$ | 0.95 | 0.94 | 0.90 | 0.90 | 0.91 | 0.96 | 0.72 | 0.89 |
| $Fe^3$ | 0.01 | 0.03 | 0.00 | 0.00 | 0.11 | 0.00 | 0.00 | 0.02 |
| Mn | 0.04 | 0.05 | 0.07 | 0.08 | 0.04 | 0.03 | 0.25 | 0.06 |
| Mg | 0.00 | 0.00 | 0.00 | 0.00 | 0.00 | 0.00 | 0.00 | 0.01 |
| Ca | 0.00 | 0.00 | 0.00 | 0.00 | 0.00 | 0.00 | 0.00 | 0.02 |
| Total | 2.00 | 2.00 | 2.00 | 2.00 | 2.00 | 2.00 | 2.00 | 2.00 |

structures consisting of millimetre-thick quartz-laminae alternated with laminae composed of muscovite, rare biotite, and rare chlorite. Garnet forms anhedral to subhedral grains ranging from 0.5 to 2.0 mm in diameter and its composition is shown in Figures 4c and 5f-h and Table 2. The inspected garnet grains display a weakly developed bell-shaped spessartine profile ($X_{sps}$ decreasing from ~20 to 13) and generally U-shaped almandine profile ($X_{alm}$ increasing from ~57 to ~71). Grossular content is characterized by slightly depleted core ($X_{grs}$ ~11), enriched inner rim ($X_{grs}$ ~20), and strongly depleted outer rim ($X_{grs}$ ~6), while pyrope content is generally low and shows a weak increase towards the rim ($X_{py}$ increases from ~6 to ~9).

Garnet porphyroblasts commonly contain abundant ilmenite and staurolite inclusions. The ilmenite inclusions are typically arranged in sigmoidal inclusion trails preserved across the whole grains, while the staurolites are mostly found in garnet rims (Figure S3). Sigmoidal ilmenite inclusion trails indicate that garnet grains grew continually during non-coaxial deformation. This conclusion is additionally reinforced by frequent asymmetric, sigma-type pressures shadows developed around garnet grains.

K-white mica is dominated by the low $Si^{4+}$ variety with $Si^{4+}$ content ranging from 3.05 to 3.15 cations p.f.u. However, there is also a much less common group for which $Si^{4+}$ content ranges from 3.28 to 3.33 cations p.f.u. (Figure 6, Table 4). A few white mica grains with low $Si^{4+}$ content are characterized by $Mg^{2+}$ and $Fe^{2+}$ concentrations,

similar to phengitic mica (Table 4). This may indicate that these grains partially lost $Si^{4+}$ during the late *LP* metamorphic episode.

Plagioclase generally forms small grains ranging from 0.05 mm to 0.2 mm in diameter. In terms of chemical composition, plagioclase grains range in composition from oligoclase to andesine with maximum 36 mol% An (Table 5).

Staurolite forms both inclusions within garnet as well as abundant matrix grains. The staurolite grains in the matrix are elongated parallel to the penetrative foliation and range in length from 0.05 to 0.6 mm. It is characterized by $X_{Mg}$ between 0.10 and 0.13 (Table 8). We have also observed sigmoidal inclusion trails of ilmenite within staurolite crystals.

Small biotite flakes were documented in the matrix of the inspected PK033 micaschist sample. Biotite composition is characterized by $X_{Mg}$ varying from 0.43 to 0.45 (Table 6).

Based on textures and mineral composition, we distinguish two mineral assemblages in the PK033 sample. The M1 assemblage is represented by the occasional phengitic white mica (Ph), with relatively high $Si^{4+}$ corresponding to a possible high-*P* history of the rock. The M2 assemblage comprises Grt + Ms + Bt + St + Pl+ Chl +Ilm + Qz. The sigmoidal ilmenite inclusions preserved both in the garnet and staurolite blasts testify to their syndeformational growth with respect to non-coaxial deformation phase.

**TABLE 8** Representative EMP analyses of staurolite grains in investigated micaschist PK033 (oxides in wt.%, cation in a pfu). $X_{Fe} = Fe/(Fe + Mg)$

| Sample | PK033 | PK033 | PK033 | PK033 | PK033 | PK033 | PK033 | PK033 | PK033 | PK033 | PK033 | PK033 | PK033 | PK033 |
|---|---|---|---|---|---|---|---|---|---|---|---|---|---|---|
| $SiO_2$ | 27.55 | 27.82 | 28.32 | 27.74 | 28.52 | 28.11 | 28.18 | 27.85 | 28.21 | 28.32 | 27.61 | 27.93 | 27.55 | 28.19 |
| $TiO_2$ | 0.77 | 0.61 | 0.54 | 0.72 | 0.38 | 0.41 | 0.45 | 0.46 | 0.48 | 0.46 | 0.39 | 0.30 | 0.63 | 0.50 |
| $Al_2O_3$ | 54.61 | 54.98 | 54.38 | 54.73 | 54.90 | 54.86 | 54.80 | 55.29 | 54.59 | 54.69 | 54.80 | 55.45 | 55.11 | 54.58 |
| $FeO$ | 12.86 | 12.45 | 11.97 | 12.54 | 12.35 | 12.36 | 12.35 | 12.83 | 12.34 | 12.01 | 12.40 | 12.62 | 12.43 | 12.11 |
| $MnO$ | 0.47 | 0.51 | 0.33 | 0.29 | 0.37 | 0.45 | 0.41 | 0.44 | 0.39 | 0.62 | 0.63 | 0.43 | 0.48 | 0.43 |
| $MgO$ | 0.88 | 0.91 | 0.90 | 0.79 | 1.01 | 0.97 | 0.94 | 0.92 | 0.97 | 1.00 | 0.82 | 0.77 | 0.82 | 0.94 |
| $CaO$ | 0.00 | 0.01 | 0.00 | 0.03 | 0.01 | 0.00 | 0.00 | 0.00 | 0.02 | 0.00 | 0.03 | 0.00 | 0.00 | 0.00 |
| $Na_2O$ | 0.08 | 0.00 | 0.01 | 0.03 | 0.05 | 0.00 | 0.03 | 0.03 | 0.02 | 0.00 | 0.06 | 0.00 | 0.00 | 0.03 |
| $K_2O$ | 0.01 | 0.01 | 0.00 | 0.00 | 0.00 | 0.01 | 0.00 | 0.00 | 0.00 | 0.00 | 0.01 | 0.01 | 0.00 | 0.00 |
| Total | 97.23 | 97.30 | 96.45 | 96.87 | 97.59 | 97.17 | 97.16 | 97.82 | 97.02 | 97.10 | 96.75 | 97.51 | 97.02 | 96.78 |
| Si | 7.66 | 7.74 | 7.88 | 7.72 | 7.93 | 7.82 | 7.84 | 7.75 | 7.85 | 7.88 | 7.68 | 7.77 | 7.66 | 7.84 |
| Ti | 0.16 | 0.13 | 0.11 | 0.15 | 0.08 | 0.09 | 0.09 | 0.10 | 0.10 | 0.10 | 0.08 | 0.06 | 0.13 | 0.10 |
| Al | 17.91 | 18.03 | 17.83 | 17.94 | 18.00 | 17.99 | 17.97 | 18.13 | 17.90 | 17.93 | 17.97 | 18.18 | 18.07 | 17.90 |
| $Fe^{2+}$ | 2.99 | 2.90 | 2.78 | 2.92 | 2.87 | 2.88 | 2.87 | 2.98 | 2.87 | 2.79 | 2.88 | 2.94 | 2.89 | 2.82 |
| Mn | 0.11 | 0.12 | 0.08 | 0.07 | 0.09 | 0.11 | 0.10 | 0.10 | 0.09 | 0.15 | 0.15 | 0.10 | 0.11 | 0.10 |
| Mg | 0.36 | 0.38 | 0.37 | 0.33 | 0.42 | 0.40 | 0.39 | 0.38 | 0.40 | 0.41 | 0.34 | 0.32 | 0.34 | 0.39 |
| Ca | 0.00 | 0.00 | 0.00 | 0.01 | 0.00 | 0.00 | 0.00 | 0.00 | 0.01 | 0.00 | 0.01 | 0.00 | 0.00 | 0.00 |
| Na | 0.04 | 0.00 | 0.01 | 0.02 | 0.03 | 0.00 | 0.02 | 0.02 | 0.01 | 0.00 | 0.03 | 0.00 | 0.00 | 0.02 |
| K | 0.00 | 0.00 | 0.00 | 0.00 | 0.00 | 0.00 | 0.00 | 0.00 | 0.00 | 0.00 | 0.00 | 0.00 | 0.00 | 0.00 |
| Total | 29.25 | 29.29 | 29.06 | 29.15 | 29.42 | 29.28 | 29.28 | 29.46 | 29.23 | 29.26 | 29.15 | 29.37 | 29.21 | 29.17 |
| $X_{Fe}$ | 0.89 | 0.88 | 0.88 | 0.90 | 0.87 | 0.88 | 0.88 | 0.89 | 0.88 | 0.87 | 0.89 | 0.90 | 0.89 | 0.88 |
| $X_{Mg}$ | 0.11 | 0.12 | 0.12 | 0.10 | 0.13 | 0.12 | 0.12 | 0.11 | 0.12 | 0.13 | 0.11 | 0.10 | 0.11 | 0.12 |
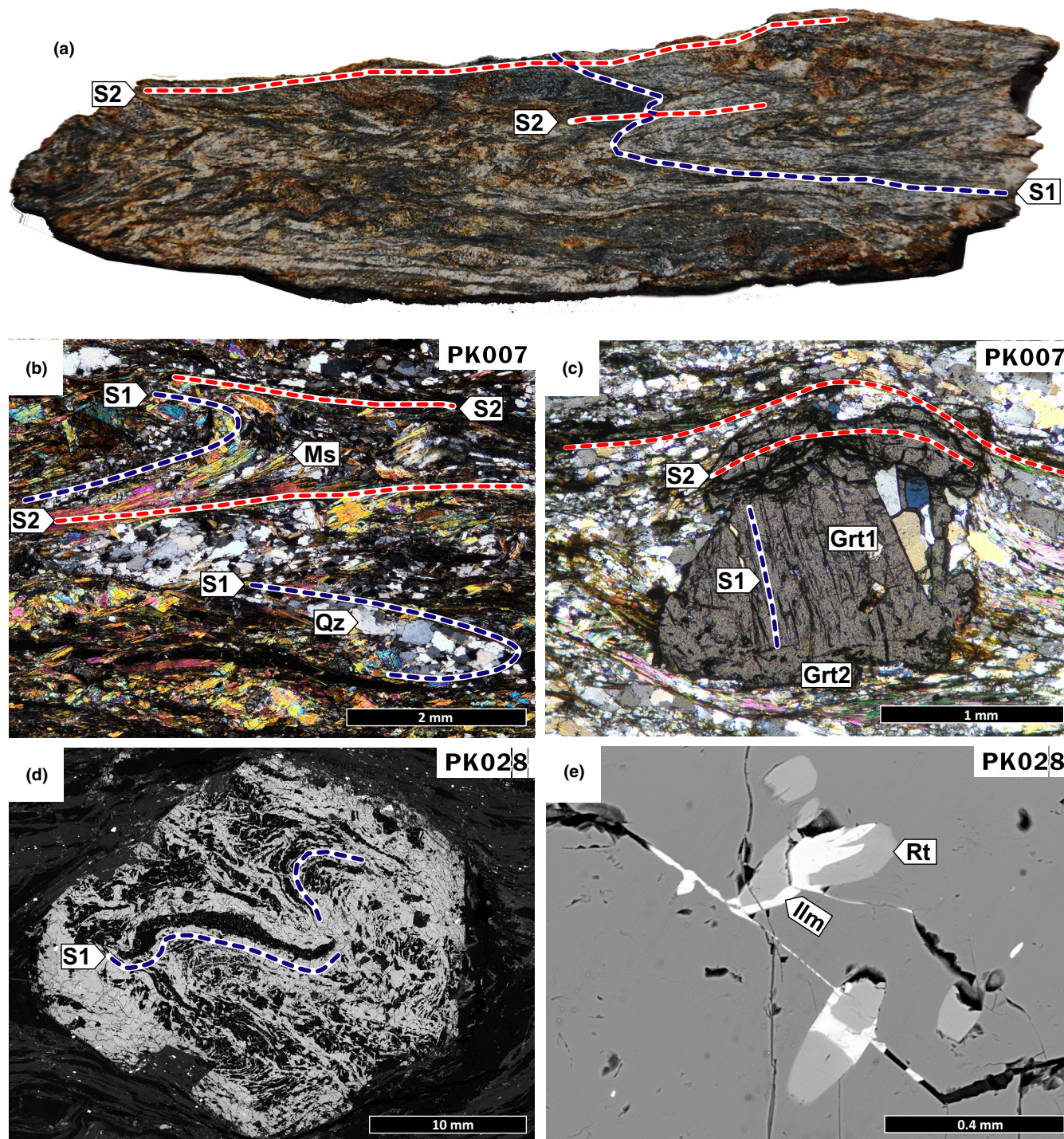
**FIGURE 2** Photograph (a) and microphotograph (b) showing two sets of foliations preserved in sample PK007. The older planar structure S1 is refolded. (c) Microphotograph showing a complex garnet porphyroblast in sample PK007 with inclusion trails composed of rutile corresponding to S1 foliation (blue dashed lines) in its inner part (Grt1), and S2 foliation (red dashed lines), composed of mostly ilmenite, preserved in its rim part (Grt2) and also in the matrix of the rock. (d) Backscattered electron image showing inclusion trails preserved in garnet porphyroblast from sample PK028: S1 folded foliation (blue dashed lines). (e) Backscattered electron image showing ilmenite replacing primary rutile inclusions in a garnet porphyroblast from sample PK028
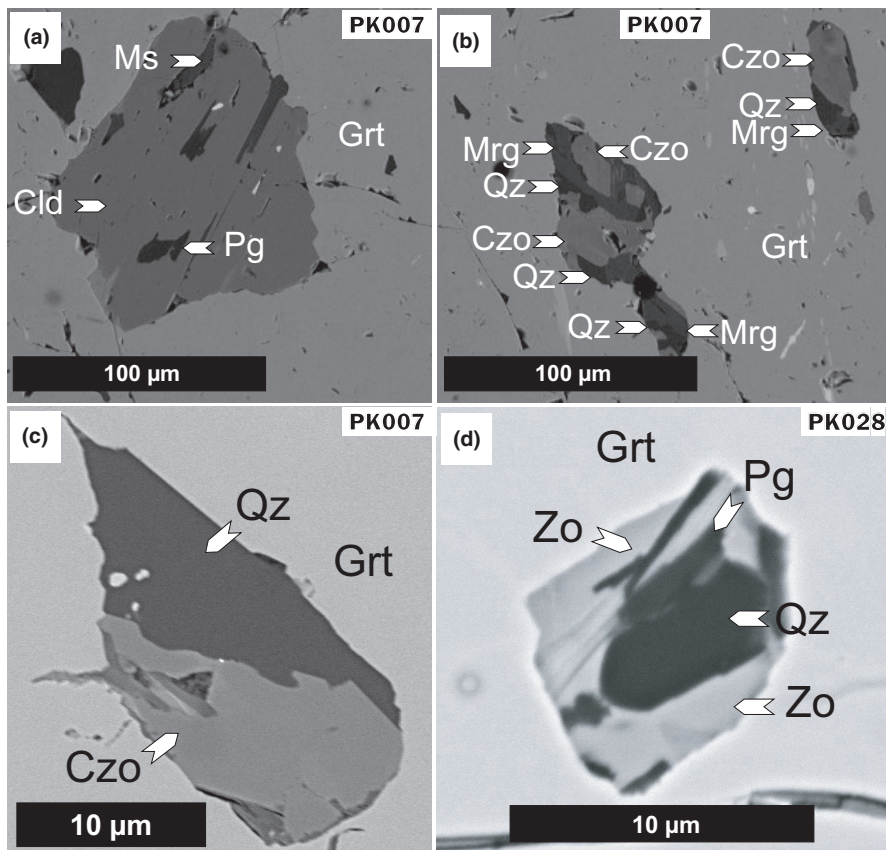
**FIGURE 3** Backscattered electron images showing the textures of polymineralic inclusions in garnets: (a)–(c) from sample PK007. (a) Polymineralic inclusion consisting of Ctd + Ms + Pg; (b) polymineralic inclusions composed of Mg + Qz + Czo; (c) Polymineralic inclusion composed of Czo + Qz, (d) Polymineralic inclusion composed of Zo + Pg + Qz

# 5 | PHASE EQUILIBRIA AND *P–T* EVOLUTION

## 5.1 | Sample PK007

An isochemical phase diagram calculated based on bulk rock composition reveals two regions of intersecting isopleths constructed for the garnet core composition: (I) ~18 kbar and ~470℃ and (II) ~5 kbar and ~520℃ (Figure S4, green circle). However, only the first region is located within the stability field of Grt + Ph +Pg + Cld + Lws + Chl + Rt + Qz, which is compatible with the inclusion set observed in the inspected garnet grains. Therefore, we chose 440℃ and 20 kbar as a starting point for our *P–T* path calculation for Grt1 (Figure S4). In sample PK007, garnet are characterized by major compositional changes over very short distance between their core and rim parts. Therefore, it is problematic to model the entire *P–T* history along the garnet profiles from this sample using the approach proposed by Moynihan and Pattison (2013), as the applied search routine is not capable of accommodating large differences in *P–T* space (see Catlos et al., 2018). Thus, we decided to separately model the *P–T* history of the core (Grt1) and rim (Grt2) parts. The obtained *P–T* paths and a comparison of observed and modelled garnet chemical profiles are presented in Figure 7.

The generally prograde *P–T* path for Grt1 is rather irregular. It starts at 468℃ and 18.1 kbar and ends at 490℃ and 18.3 kbar resulting in a temperature increase of ~22℃ and pressure variations of 0.9 kbar (Figure 7a). According to thermodynamic modelling, the core part of garnet grain (Grt1) in this sample was equilibrated within the stability field of Grt + Ph + Pg + Cld + Lws + Chl +Rt + Qz, which is consistent with the observed set of inclusions and presumed Lws pseudomorphs preserved in garnet grains (Figure 8).

Results of thermodynamic modelling clearly indicated that during the *HP* stage lawsonite should be present in a relatively small amount, only slightly exceeding 2 vol%. Furthermore, $X_{Mg}$ of chloritoid should fall in the range of 0.1–0.14, which agrees well with the observed composition of this mineral (Figures 8d,e and 9b).

The effective bulk rock composition calculated at the end of Grt1 growth was used as an input for reconstructing of *P–T* conditions during Grt2 growth (Table 9). The calculated isochemical phase diagram (Figure S5) shows that garnet compositional isopleths intercept at both high-*P* and low-*P* portion of the analysed *P–T* space (19 kbar at 480℃ and 5.2 kbar at 535℃). However, only the low-*P* intersection is located within the ilmenite stability field and outside the stability fields of rutile, lawsonite, and chloritoid. Thus, the low-*P* field is in agreement with the observed set of mineral inclusion preserved in Grt2. Therefore, we
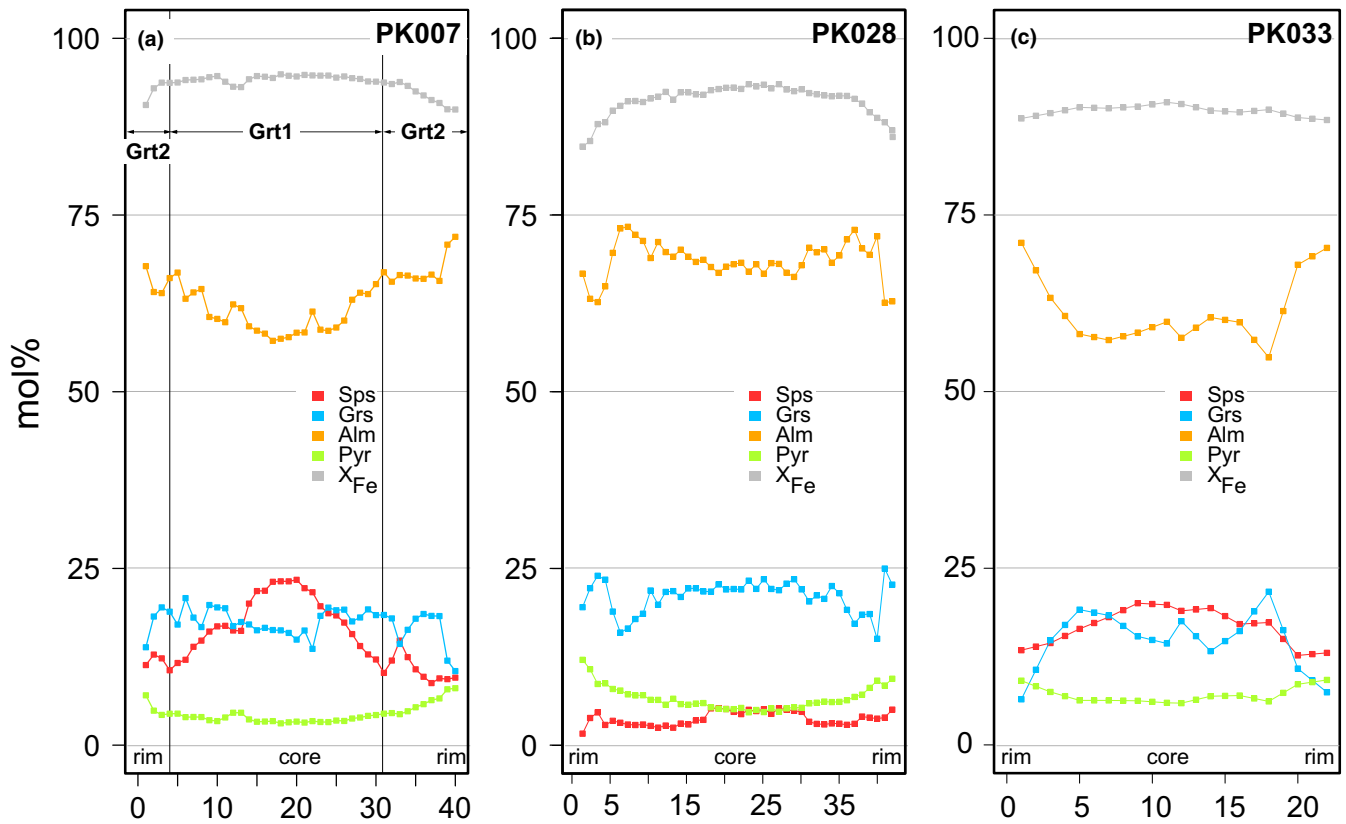
**FIGURE 4** Chemical zoning of representative garnet grains. (a) Sample PK007, (b) sample PK028, (c) sample PK033. $X_{Fe} = Fe/(Fe + Mg)$

chose 532℃ and 5.18 kbar as a starting *P–T* condition for calculations performed for Grt2 growth (Figure S5, green circle). The reconstructed prograde *P–T* path is located in low-*P* region of the analysed *P–T* space at 538–568℃ and 5.7–7.1 kbar (Figure 7a). As a result, the core of Grt2 was equilibrated in the stability field of Grt + Pl + Bt + Ms + Chl + Ilm (Figure 9d). This mineral assemblage is compatible with commonly preserved ilmenite inclusions in Grt2, as well as plagioclase observed in the matrix of the sample. Pressure and temperature differences during the transition between Grt1 and Grt2 yield ~13 kbar and ~50℃ (Figure 7a). According to our thermodynamic modelling, the simplest explanation for strongly limited garnet growth at the transition between Grt1 and Grt2 is that reconstructed *P–T* path is nearly parallel to garnet vol% isopleths (Figure 9c). A fast decompression rate may be an additional factor suppressing garnet growth at this stage. Unfortunately, this is only a speculation as the grains of both garnet types are too small to be separately dated to test this hypothesis.

The *P–T* path reconstructed based on the Grt2 composition ends in the stability field of Pl2 + Grt + Bt + Ms + Chl + Ilm (Figure 9f). However, the reconstructed *P–T* path may constitute an incomplete record of garnet growth. A careful inspection of the chemical profiles shows a slight spessartine increase in the outer rim (Figure 4a), and garnet grains from

this sample show very irregular shapes (Figure 5a, S1 and S2). Both observations are indicative of partial garnet resorption, which could be responsible for the partial dissolution of garnet grains.

## 5.2 | Sample PK028

Two regions (I and II) of intersecting isopleths for the garnet core composition can be observed in an isochemical phase diagram calculated using the bulk rock composition of sample PK028 (Figure S6). The high-*P* and low-*T* region I is located outside the stability fields of lawsonite, chloritoid, and ilmenite and within the stability field of rutile. Region II is located outside the stability field of rutile, while this mineral commonly forms inclusions in garnet grains in this sample. Therefore, we use as the initial condition for *P–T* calculations point at 373℃ and 13.5 kbar, which is located close to region I of intersecting isopleths (Figure S6, green circle).

The chemical profile of the analysed garnet grain (Figure 4b) is characterized by fluctuations in grossular and almandine composition in particular. Therefore, we decided to use a simple linear regression model to smooth our data. This approach helps to maintain computational stability and faster fits with the search routine of the program. Furthermore, as is shown by Catlos et al. (2018) has
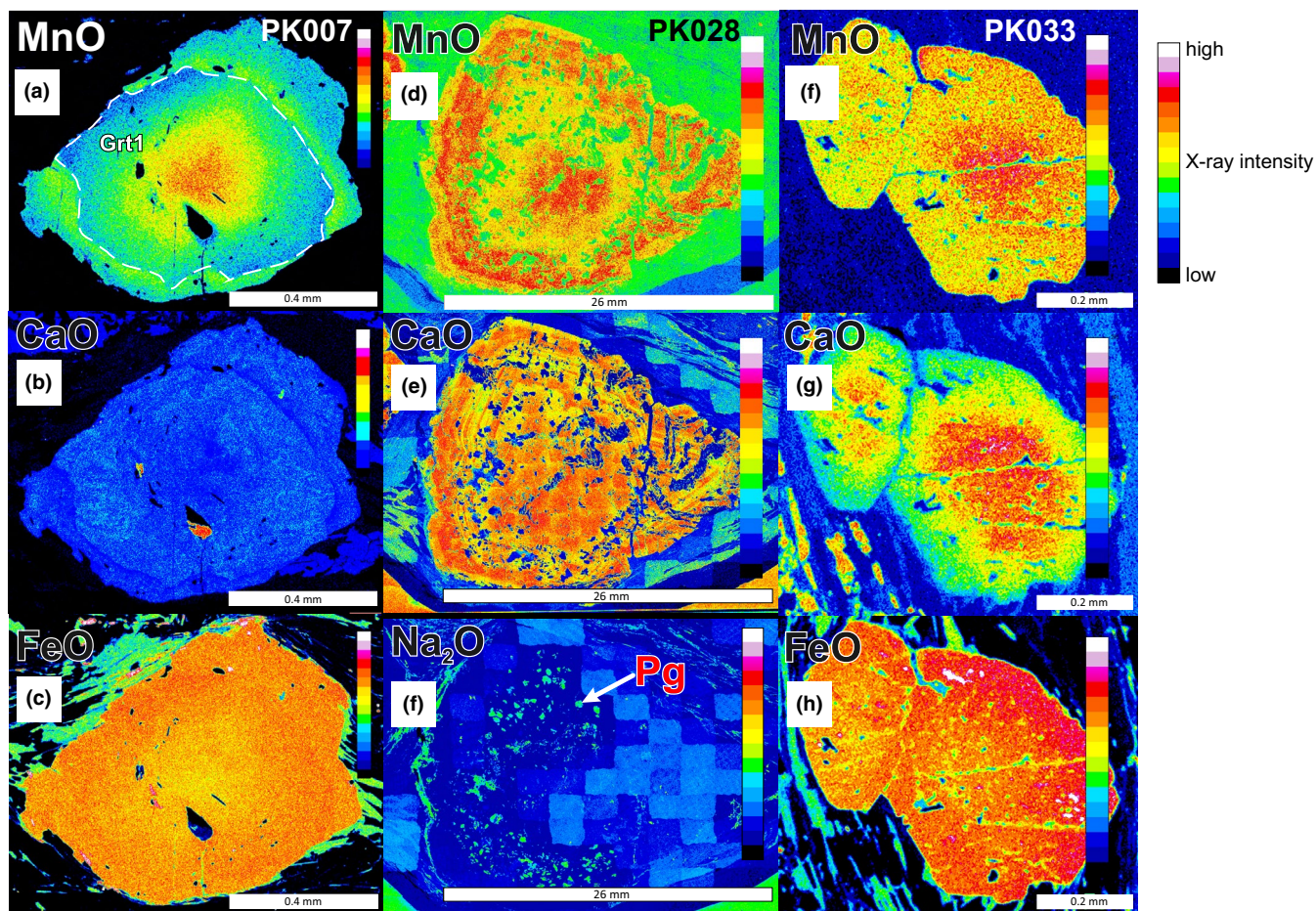
**FIGURE 5** X-Ray maps showing zoned garnet porphyroblasts from the inspected mica schists. (a)–(c) Sample PK007; (d)–(f) sample PK028; (f)–(h) sample PK033

no influence on the shape of the calculated *P–T* path. A comparison of the observed and smoothed garnet chemical profile is presented in Figure S7e. The obtained *P–T* path and a comparison of observed and modelled garnet chemical profiles are presented in Figure 10.

The first point calculated in the modelled *P–T* path is located at 502°C and 14.8 kbar, within the stability field of Grt + Bt + Pg + Ms + Chl + Cpx + Rt + Qtz—a mineral assemblage that, besides clinopyroxene, is observed in the thin section (Figure 11a and b). The reconstructed *P–T* path ends at 15.6 kbar and 567°C, in the stability field of Grt + Pl + Bt + Ms + Cpx + Rt + Qtz (Figure 11d). An isochemical phase diagrams calculated for this *P–T* space suggest that the investigated sample resided outside the chloritoid and ilmenite stability fields during garnet crystallization (Figure 11). $Si^{4+}$ content in white mica should fall in the range of 3.28 to 3.28 (Figure 11c and S7a). Furthermore, paragonite mode should evolve from 8 vol% at the onset and the final stages of garnet formation reaching 15 vol% during growth of outer core and inner rim (Figure S7b). This explains the occurrence of relatively abundant paragonite inclusions documented in garnet (Figure 5f). According to the model predictions, clinopyroxene reached a maximum modal percentage of 9.5 vol% at the beginning of garnet growth and

dropped to ~4.5 vol% when garnet growth ceased (Figure S7d). This poses a question concerning clinopyroxene traces or its decomposition products preserved in the garnet. We speculate that the breakdown of clinopyroxene might have resulted in additional paragonite and plagioclase inclusions relatively abundantly preserved in garnet porphyroblasts according to one or more of the following reactions:

$$Jd + Qtz = Ab,$$

$$5Jd + 6Czo + 2H_2O = 4Grs + 5Pg + Qtz,$$

$$Jd + 2Czo = An + Grs + Pg,$$

$$6Jd + 6Czo + 2H_2O = Ab + 4Grs + 5Pg.$$
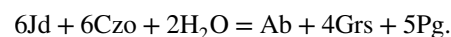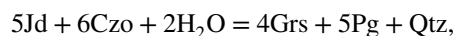
Interestingly, the results of thermodynamic modelling clearly indicate that at the beginning of garnet formation the only stable Ti-bearing phase is rutile, while at the final stages of garnet crystallization ilmenite is formed (Figure S7c). All these modelling results are in agreement with the observed set of mineral inclusions and their textural relations observed in garnet grains.

## 5.3 | Sample PK033

The isochemical phase diagram constructed for sample PK033 shows two regions of intercepting isopleths that correspond to the garnet core composition: (I) 18 kbar and 470℃ and (II) 4.8 kbar and 518℃ (Figure S8). Only the second region
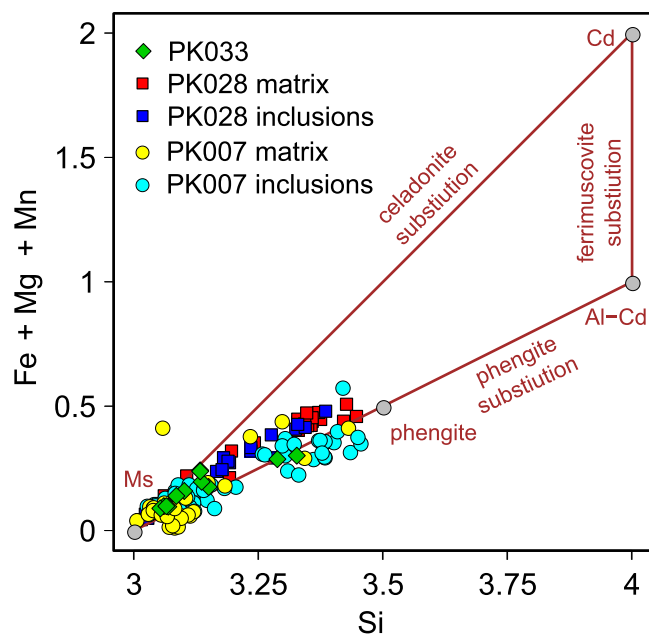


**FIGURE 6** Compositional variations of white micas in the investigated mica schists from the Kamieniec Metamorphic Belt

is located within the stability field of the mineral assemblage comprising Grt + Ms + Bt + Pl + Chl + Ilm + Qz that is observed both in the matrix and as inclusions in the garnet grains. Therefore, we chose 496℃ and 3.5 kbar as a starting point for the P–T path calculation (Figure 12a, green circle). The obtained P–T path and a comparison of observed and modelled garnet chemical profiles are presented in Figure 12.

The obtained, generally prograde path ranges in the P–T space from ~4.7 kbar and ~530℃ to ~5.3 kbar and 550℃, resulting in a pressure variation of 0.6 kbar and a temperature increase of ~20℃ (Figure 12a). According to thermodynamic modelling, the rims of garnet grains in this sample were equilibrated within the stability field of Grt + Ms + Bt + Pl + St + Chl + Ilm + Qz (Figure 13). This is in accordance with both the set of inclusions observed in the rim parts of garnet grains and the mineral assemblages documented in the matrix of the inspected sample.

This sample contains a few white mica grains with a relatively high $Si^{4+}$ content ranging from 3.28 to 3.33 cations p.f.u. For a crystallization temperature of 450–500℃, these grains could be equilibrated at pressures of up to 16–18.5 kbar (Figure 13c). At these P–T conditions, a stable mineral assemblage comprises Grt + Pg + Ms + Lws + Chl + Cld + Rt + Qz. We did not manage to document the mentioned HP mineral assemblage in this sample. However, according to the thermodynamic modelling, the amount of both paragonite and chloritoid should not exceed 5–8 vol% each. Furthermore, lawsonite volume should be less than 1.5 vol%
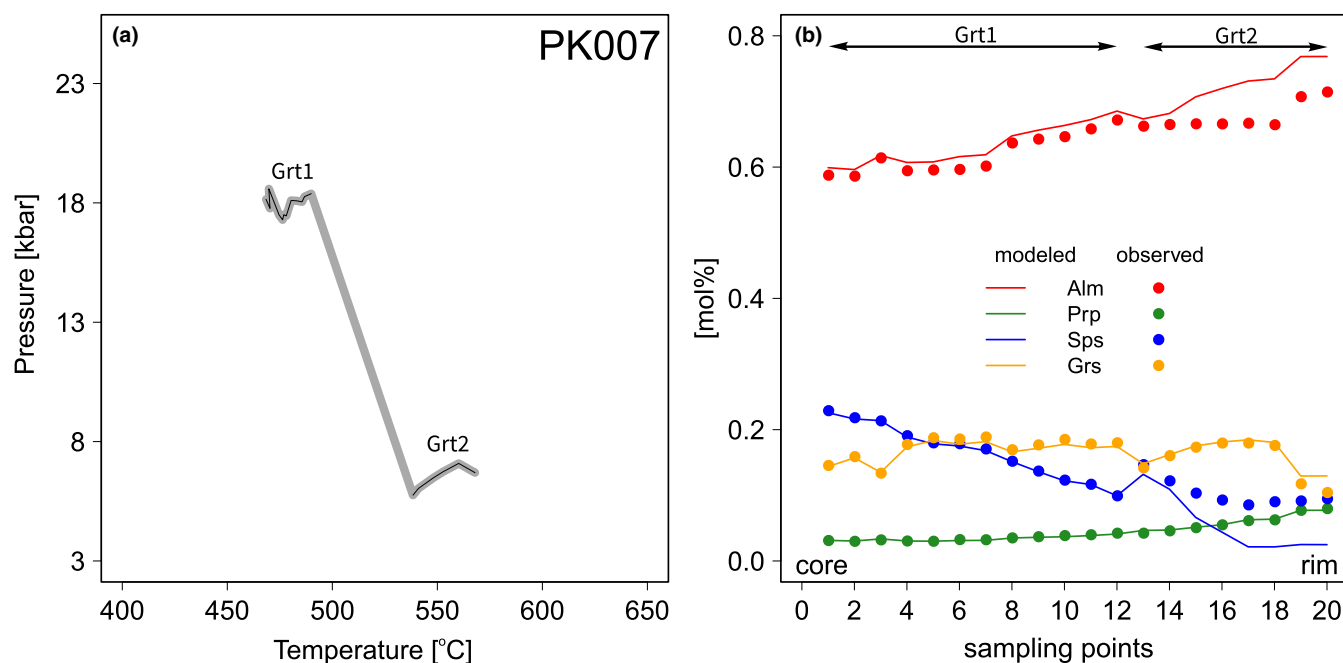


**FIGURE 7** Results of thermodynamic modelling for sample PK007: (a) reconstructed P-T path, (b) modeled versus measured chemical profiles in garnet. A core to rim sector of the profile was analysed. Numbers on X axis denote consecutive sampling points in garnet grain. Profile length 0.47 mm

at 500℃, and at 550℃ this mineral phase is not stable. The relatively minor amounts of these *HP* minerals could easily be obliterated during retrogression.

To reconstruct the *P–T* history of the investigated samples from the KMB, we have also applied a method proposed by Evans (2004) and the thermodynamic database of Berman (file JUN92d.bs, Berman, 1988) as well as the brute force method of Vrijmoed and Hacker (2014). In the case of the brute force method we utilized the same set of activity models as for the method proposed by Moynihan & Pattison, 2013. Results of these calculations can be found in the supplementary file (Figures S9-S14). These calculations demonstrate that regardless of the thermodynamic database, solid solution model for minerals and the modelling approach used, both the shape and location of the calculated *P–T* paths are similar.

# 6 | QUARTZ-IN-GARNET RAMAN BAROMETRY

Fully entrapped quartz inclusions in crack-free garnet host have been measured with Raman spectroscopy. The thicknesses of the thin sections were between 40 and 60 μm and the radii of the inclusions were typically between 2 and 5 μm (Figure S15). The distance between the inclusion and the thin-section surface was at least 10 μm as estimated by focusing on the thin-section surface and then gradually moving downward to focus on the inclusion. The wavenumber shifts of the 128 and 464 cm$^{-1}$ bands compared to a quartz standard were used to infer the residual quartz inclusion pressure. The maximal wavenumber shift of 464 cm$^{-1}$ band was 5.7 cm$^{-1}$ for sample PK028, 4.5 cm$^{-1}$ for PK007 and 1.6 cm$^{-1}$ for PK033. The wavenumber differences of Raman peaks between pressurized quartz inclusion and quartz standard are provided in supplementary material (Supplementary Tables) together with calculated residual pressure based on the calibrations from Schmidt and Ziemann (2000). The converted pressures based on 128 and 464 cm$^{-1}$ peaks were very consistent for all the three samples (Figure 14a). The converted maximal residual pressures were 6.4 kbar for sample PK028, 5.0 kbar for PK007, and 1.8 kbar for PK033 (Tables S1-S3). For PK028, the highest residual inclusion pressure was found at the rim of the garnet, while the highest pressure at the garnet core was ~0.5 kbar lower than at the rim. For PK033, no difference in residual quartz inclusion pressure was observed between the garnet core and rim. For sample

PK007, it was difficult to distinguish the true core and rim due to small size of garnet transected within the thin section. Meanwhile, quartz inclusions were not abundant in the studied thin section of PK007. Therefore, we could not confirm whether there was any systematic difference between the residual quartz inclusion pressure between the garnet core and rim of PK007. In all the three samples, a wide scatter of residual pressures from negative to the maximal pressure was observed.

We used the 1D isotropic elastic model from Guiraud and Powell (2006) to recover the entrapment pressure conditions as shown in Figure 14. A MATLAB script was used to solve the equation iteratively. The PVT relationship for quartz was based on the EoS of curved alpha–beta transition by Angel et al. (2017) and for almandine/grossular/pyrope garnet it was based on Milani et al. (2015). Spessartine garnet was based on Gréaux and Yamada (2014). The volume of garnet mixture was calculated based on the molecular percentage of garnet endmembers. Using the maximal quartz inclusion pressure to recover the entrapment pressure conditions, the results show that at ~500–550℃, the entrapment pressure is ~15–16 kbar for PK028 rim, ~14–15 kbar for PK028 core, ~12–14 kbar for PK007, and ~7–8 kbar for PK033 (Figure 14b).

# 7 | CLASSICAL GEOTHERMOBAROMETRY BASED ON WHITE MICA AND GARNET CHEMISTRY

According to thermodynamic modelling, the core and rim parts of garnet grains in the sample PK007 were formed in contrastingly different *P–T* conditions. This is confirmed by the diverse inclusion sets preserved in various parts of these garnet grains, including white mica. The muscovite grains in both PK007 and PK028 samples display variable chemical composition, varying from phengite to K-white mica with low Si$^{4+}$ content and paragonite. In the sample PK033, white mica shows a rather homogenous composition typical for K-white mica with mostly low Si$^{4+}$ content (Table 4). However, we also documented a few grains showing a more phengitic composition (Table 4). To estimate the *P–T* conditions of white mica formation in all the analysed samples, we have applied Si$^{4+}$ in phengite geobarometer (Kamzolkin et al., 2016) coupled with Ti$^{4+}$ in white mica geothermometer (Wu & Chen, 2015). The advantage of these tools is that they

**FIGURE 8** Phase diagram modeling results for sample PK007 using the core composition of Grt1 and bulk rock composition (a) isochemical phase diagram (b) isopleths shown for mole fraction of almandine (red), grossular (blue), and spessartine (purple). Mole fraction isopleths are shaded using 0.01 intervals. The stability fields of garnet, clinopyroxene, chloritoid, lawsonite, plagioclase, ilmenite and rutile are additionally shown. (c) Compositional isopleths of Si$^{4+}$ in K-white mica (pfu, based on 11 oxygens). d) Compositional isopleths of the $X_{Mg}$ in chloritoid. e) vol% isopleths for lawsonite. Yellow areas mark the intersection of isopleths
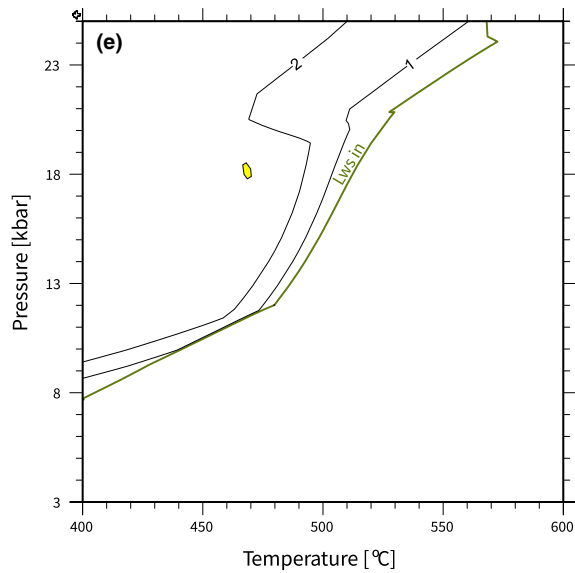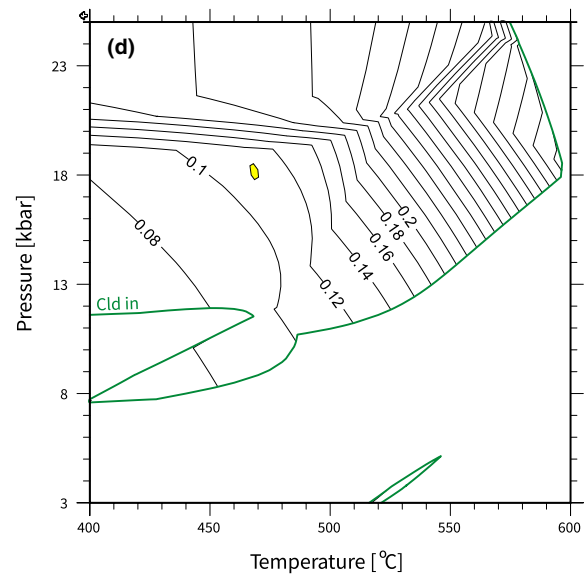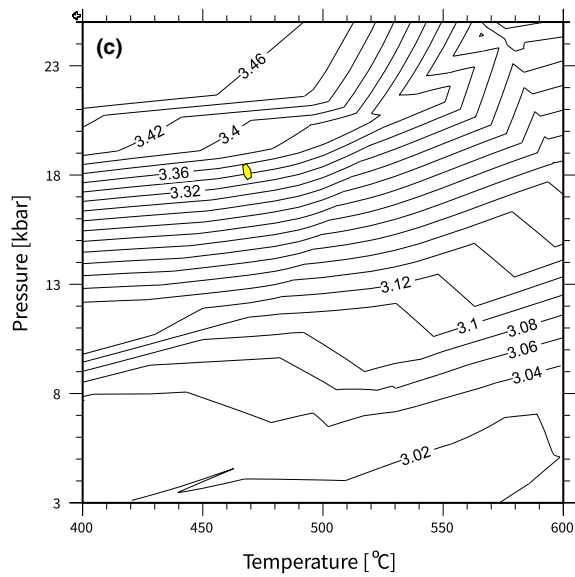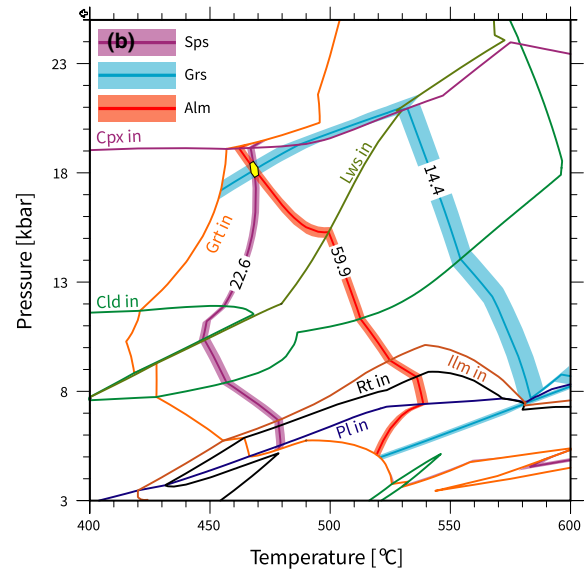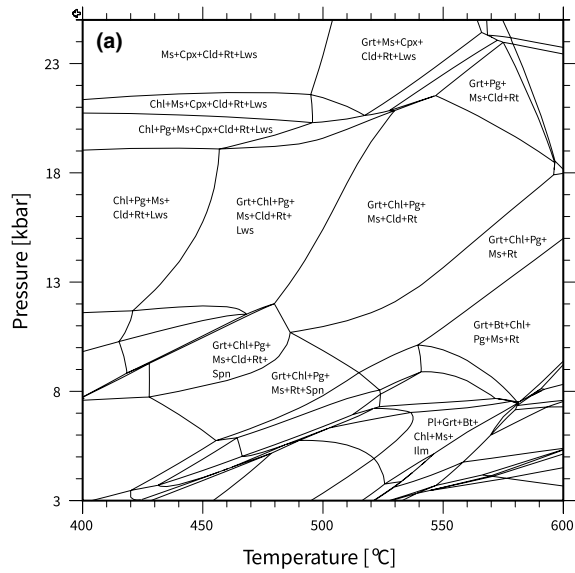
are based on the composition of the same mineral. However, the $Ti^{4+}$ in white mica geothermometer was calibrated for a low-*P* mineral assemblage comprising ilmenite and sillimanite, and the latter mineral is not present in the inspected samples. Therefore, we have supplemented these calculations by applying two calibrations for the garnet–muscovite geothermometer formulated for metapelites metamorphosed at high pressures (Green & Hellmann, 1982; Hynes & Forest, 1988). The results of geothermobarometric calculations are presented in Figure 15.

The PK007 and PK028 samples are characterized by the occurrence of two groups of white mica. The groups considerably differ by $Si^{4+}$ content. In the micaschist PK007, the most common white mica flakes are characterized by relatively low $Si^{4+}$ contents, testifying to equilibration pressures of max ~3–7 kbar, while phengitic white mica crystallized predominantly at ~15–21 kbar depending on the applied calibration of geothermobarometers (Figure 15a). The grains with the lowest $Si^{4+}$ content were mostly documented in the cleavage zones as well as in Grt2, that is, in the rim parts of the garnet grains. Conversely, phengitic white mica grains were mostly documented in the microlithons as well as in Grt1, that is, in the core parts of garnet grains. In PK028, the phengites most commonly crystallized at ~15–23 kbar, while less abundant low $Si^{4+}$ white mica were equilibrated at max ~10 kbar (Figure 15b). In the PK033 sample, most white mica grains were formed at pressures ranging from 5 to 8 kbar. However, a few grains were also equilibrated at higher pressures of ~15–17 kbar (Figure 15c). We suggest that the observed bimodal distribution of $Si^{4+}$ content in white mica may be a record of *LP* overprint of earlier *HP* metamorphic event. The *LP* event is not recorded by garnet but is preserved in white mica (Figures 8c, 9e, 11c, 13c).

Results of classical geothermobarometry clearly indicate that two compositional groups of white mica that were formed at strikingly different *P–T* conditions are present in the investigated samples. This is especially obvious for sample PK007 for which the estimated *P–T* conditions of white mica crystallization are quite consistent with the formation conditions of two garnet generations (Grt1 and Grt2) as based on thermodynamic modelling. Importantly, especially in the case of the sample PK007 phengitic white

mica were observed exclusively in Grt1, while low $Si^{4+}$ muscovites were documented in Grt2. However, comparison of the results obtained using classical geothermobarometry and thermodynamic modelling suggests that muscovite–garnet geothermometer in calibration of Green and Hellmann (1982) and Ti-in-muscovite geothermometer of Wu and Chen (2015) may overestimate temperatures. As a consequence, the predicted pressure based on these geothermometers are also overestimated. The two K-white mica compositional groups are also present in the remaining two samples PK028 and PK033. In PK028 low $Si^{4+}$ mica group equilibrated at pressures not exceeding 10 kbar is particularly interesting. Its occurrence implies a significant pressure drop to values of ~3–10 kbar after garnet formation.

The pressure estimates based on classical geothermobarometry are in good agreement with inferences drawn from the Raman data and the calculated isochemical phase diagrams. The only notable discrepancy is that white mica with high $Si^{4+}$ content observed in samples PK007 and PK028 exhibit pressures higher by ~2–4 kbar as compared to the *P–T* estimates based on garnet zoning.

# 8 | DISCUSSION

## 8.1 | Peak metamorphic conditions and implications for regional geology

The Kamieniec Metamorphic Belt has not been, up to now, recognized as bearing a pervasive imprint of *HP–LT* metamorphism. *HP* metabasites have been described in the KMB (Achramowicz et al., 1997; Bakun-Czubarow, 1998), but until recently little attention had been paid to the associated widespread metapelites and their high-*P* record. Our work demonstrates the significance of metapelites in the study of *HP* metamorphism of the KMB. Our data indicate that rocks of the KMB experienced a T/P gradient in the range between 25 and 38℃/kbar on their prograde path. Using the lithostatic pressure approach and taking an average density of 2.7 g/cm$^3$ for the overburden, the obtained peak pressures correspond to a geothermal gradient of ~6.9–10.4℃/km. These very low

**FIGURE 9** Phase diagram modeling results for sample PK007 using the rim composition of Grt1 and fractionated rock composition (a)–(c), the core composition of Grt2 (d)–(e), and the rim composition of Grt2 (f). (a) Isopleths shown for mole fraction of almandine (red), grossular (blue), and spessartine (purple). Mole fraction isopleths are shaded using 0.01 intervals. The stability fields of garnet, clinopyroxene, chloritoid, lawsonite, plagioclase, ilmenite and rutile are shown. (b) Compositional isopleths of the $X_{Mg}$ in chloritoid (solid line), and vol% isopleths of lawsonite (dashed line). (c) vol% isopleths of garnet. (d) Isopleths shown for mole fraction of almandine (red), grossular (blue), and spessartine (purple) with shading that spans two contour intervals of 0.01 mole fraction. The stability fields of garnet, clinopyroxene, lawsonite, plagioclase, staurolite, ilmenite and rutile are shown. (e) Compositional isopleths of $Si^{4+}$ in K-white mica (pfu, based on 11 oxygens). (f) Isopleths shown for mole fraction of almandine (red), grossular (blue), and spessartine (purple) with shading that spans two contour intervals of 0.01 mole fraction. The stability fields of garnet, clinopyroxene, chloritoid, lawsonite, plagioclase, ilmenite and rutile are shown. Yellow areas mark the intersection of isopleths
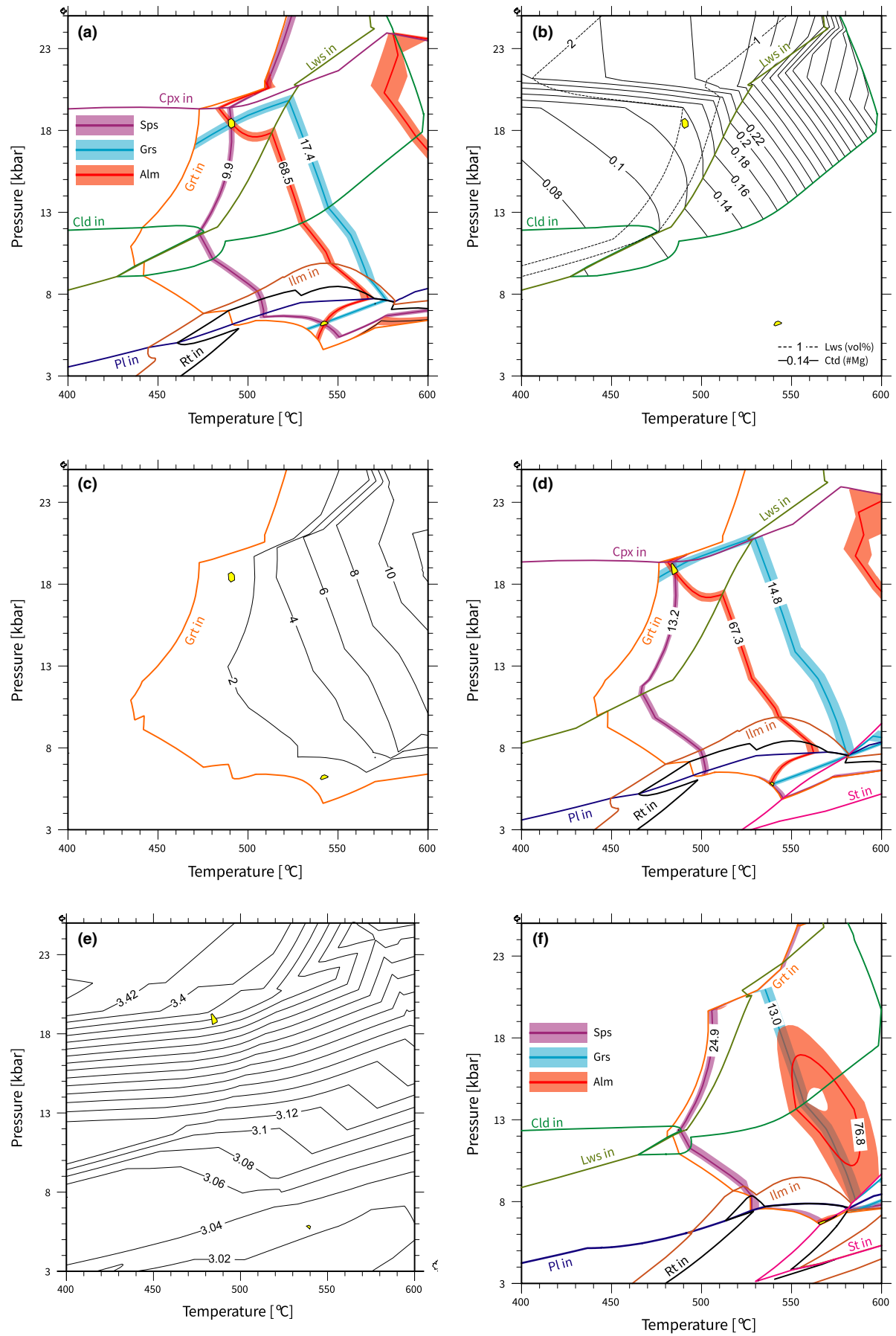
**TABLE 9** Bulk and garnet (Mod - modelled) compositional data (mol%) calculated using the MP13 method. For comparison given is also observed (Obs) compositional data for garnet used in modelling

| Sample | PK007 inner core | PK007 outer core | PK007 inner rim | PK007 outer rim | PK028 core | PK028 rim | PK033 core | PK033 rim |
|---|---|---|---|---|---|---|---|---|
| No | 1 | 12 | 1 | 8 | 1 | 18 | 1 | 21 |
| XMod_alm | 59.9 | 68.5 | 67.3 | 76.9 | 72.5 | 79.8 | 66.3 | 70.7 |
| XMod_prp | 3.1 | 4.1 | 4.7 | 7.7 | 2.3 | 5.0 | 4.1 | 6.7 |
| XMod_sps | 22.6 | 9.9 | 13.2 | 2.5 | 4.4 | 0.3 | 17.2 | 12.6 |
| XMod_grs | 14.4 | 17.4 | 14.8 | 13.0 | 20.8 | 14.9 | 12.4 | 10.0 |
| XObs_alm | 58.9 | 67.3 | 66.4 | 71.6 | 67.6 | 68.1 | 59.9 | 71.1 |
| XObs_prp | 3.3 | 4.4 | 4.4 | 8.1 | 4.6 | 12.1 | 6.0 | 9.1 |
| XObs_sps | 14.7 | 18.2 | 14.4 | 10.6 | 23.3 | 18.6 | 14.4 | 6.5 |
| Obs_Xgrs | 23.1 | 10.1 | 14.8 | 9.7 | 4.5 | 1.3 | 19.8 | 13.4 |
| $SiO_2$ | 61.16 | 60.53 | 60.47 | 59.57 | 49.78 | 46.14 | 60.75 | 60.51 |
| $Al_2O_3$ | 22.22 | 21.80 | 21.76 | 21.17 | 26.03 | 23.61 | 22.85 | 22.69 |
| $TiO_2$ | 0.63 | 0.63 | 0.63 | 0.63 | 0.77 | 0.77 | 0.81 | 0.81 |
| FeO | 4.63 | 4.23 | 4.19 | 3.54 | 7.57 | 4.83 | 5.03 | 4.87 |
| MgO | 2.46 | 2.44 | 2.43 | 2.38 | 2.77 | 2.63 | 2.49 | 2.48 |
| MnO | 0.08 | 0.05 | 0.04 | 0.01 | 0.01 | 0.00 | 0.08 | 0.05 |
| CaO | 0.54 | 0.43 | 0.42 | 0.26 | 1.40 | 0.66 | 0.60 | 0.57 |
| $Na_2O$ | 2.11 | 2.11 | 2.11 | 2.11 | 3.31 | 3.31 | 1.60 | 1.60 |
| $K_2O$ | 4.44 | 4.44 | 4.44 | 4.44 | 7.50 | 7.50 | 5.03 | 5.03 |
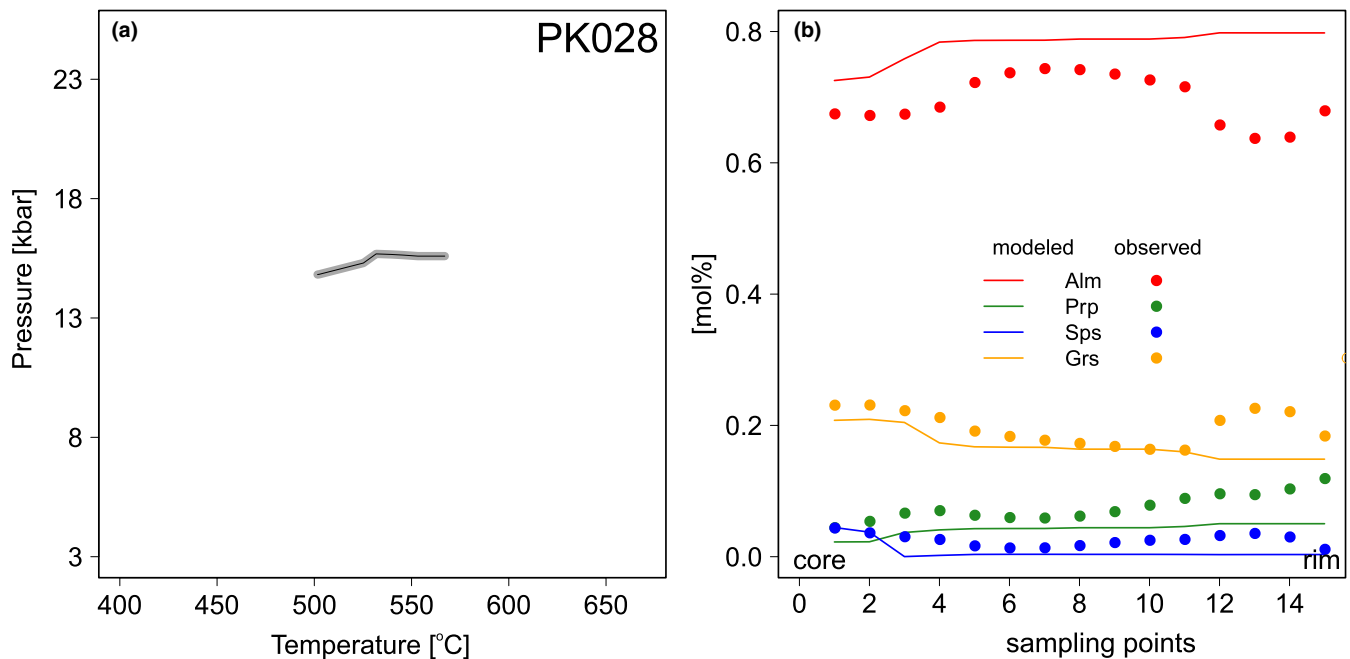


**FIGURE 10** Results of thermodynamic modelling for sample PK028: (a) reconstructed P-T path; (b) Modeled versus measured chemical profile in garnet. A core to rim sector of the profile was analysed. Numbers on X axis denote consecutive sampling points in garnet grain. Profile length 13 mm

values of geothermal gradient and the presumed presence of lawsonite indicate that the KMB was formed under _P–T_ conditions typical of a subduction zone.

The investigated samples from the Kamieniec Metamorphic Belt exhibit similar mineralogy and micro-structures, but record different aspects of the _P–T_ history
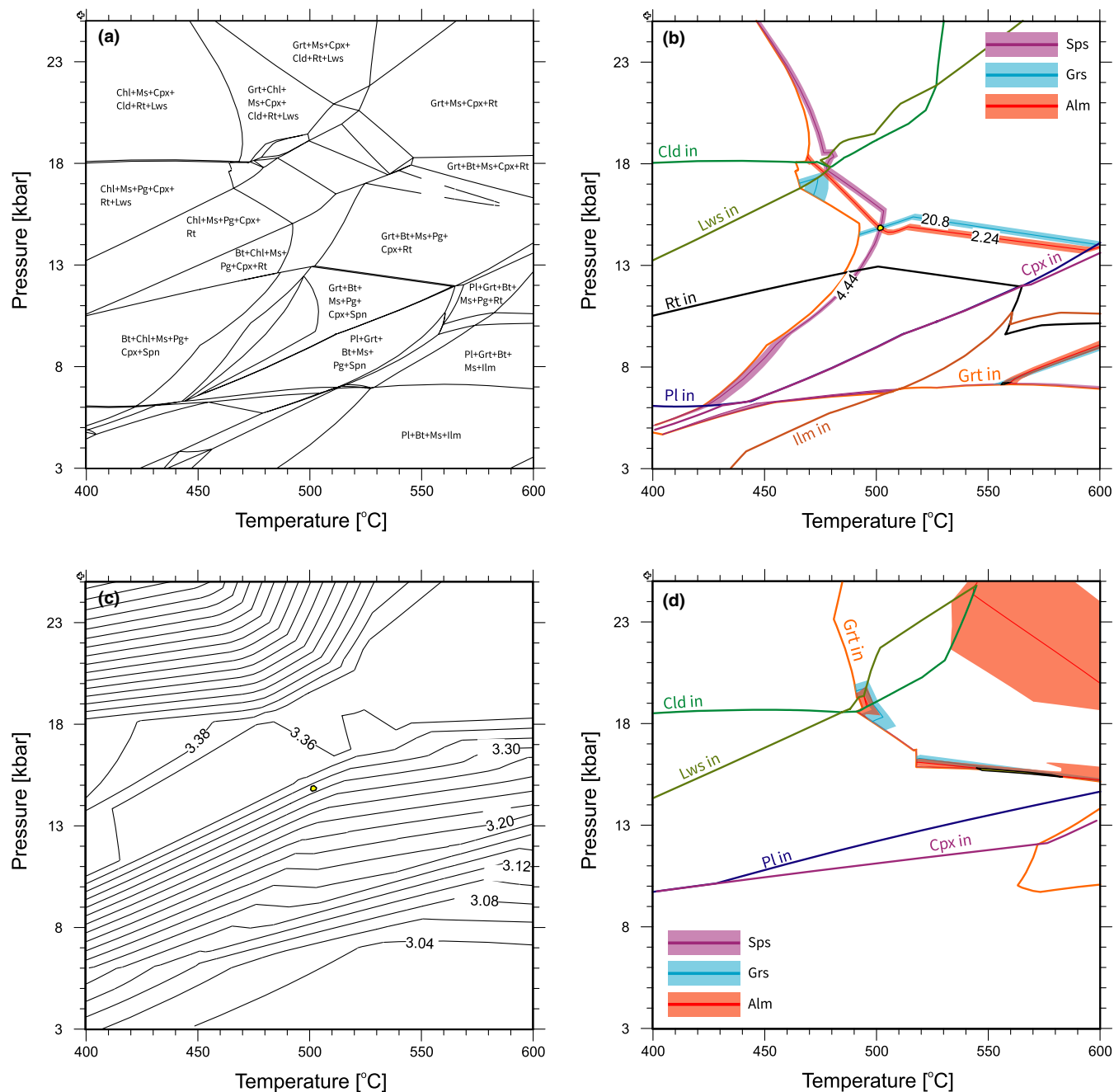
**FIGURE 11** (a) Isochemical phase diagrams for sample PK028 calculated for core composition of the analysed garnet grain. (b) Modelled isopleths for core composition of garnet shown for mole fraction of almandine (red), grossular (blue), and spessartine (purple). Mole fraction isopleths are shaded using 0.01 intervals. Additionally are shown stability fields of garnet, clinopyroxene, chloritoid, lawsonite, plagioclase, ilmenite and rutile. (c) Compositional isopleths of $Si^{4+}$ in K-white mica (pfu, based on 11 oxygens). (d) Modelled isopleths for the rim composition of garnet shown for mole fraction of almandine (red), grossular (blue), and spessartine (purple) with shading that spans two contour intervals of 0.01 mole fraction. Additionally are shown stability fields of garnet, clinopyroxene, chloritoid, lawsonite, and plagioclase. Yellow areas mark the intersection of isopleths

revealed by garnet composition, $Si^{4+}$ in phengite and quartz inclusion pressure. The micaschist PK028 sample bears a clear imprint of *HP* metamorphism, which resulted in crystallization of *HP* mineral phases such as phengitic white mica and rutile. The sample also contains K-white mica with a very low $Si^{4+}$ content and ilmenite, which both unavoidable attest to low-*P* overprint. On the other hand, the

PK033 sample is characterized by a well-preserved record of *LP* metamorphism, which is manifested by white mica with low $Si^{4+}$ content, staurolite and ilmenite. This micaschist sample also contains a few phengitic white mica grains that we interpreted as relics of *HP* conditions. The sample PK007 clearly bears a record of *HP* metamorphism overprinted by an *LP* event, with both metamorphic stages accompanied
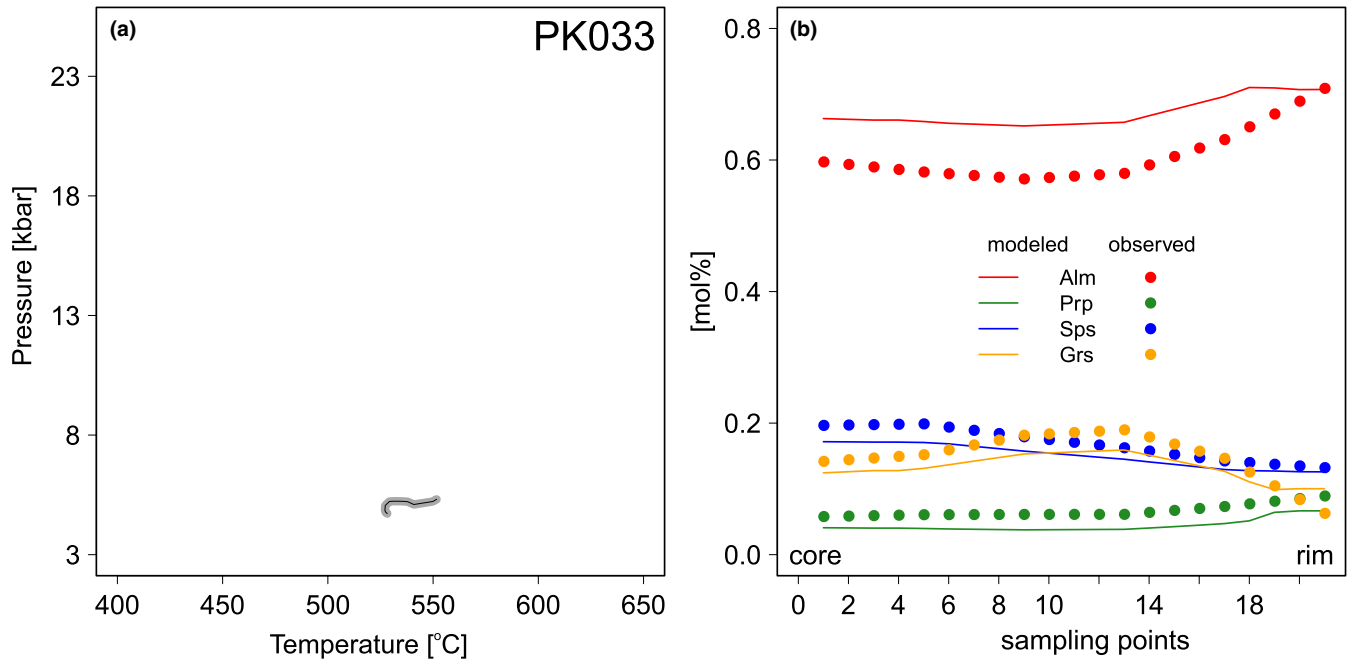
**FIGURE 12** Results of thermodynamic modelling for sample PK033: (a) reconstructed P-T path, (b) Modeled versus measured chemical profile in garnet. A core to rim sector of the profile was analysed. Numbers on X axis denote consecutive sampling points in garnet grain. Profile length 0.36 mm

by garnet growth. The early, core-forming garnet generation embeds a *HP* mineral assemblage represented by phengitic white mica, chloritoid, rutile needles, and inferred lawsonite pseudomorphs. The late, rim-forming garnet generation contains mostly ilmenite and white mica with a low $Si^{4+}$ content. Consequently, comparison of results of classical geothermobarometry and thermodynamic modelling demonstrates that most probably all the investigated samples from the KMB share the same or a similar metamorphic evolution that includes the *HP/LT* episode at ~15–18 kbar and ~470–570℃, followed by decompression to ~5–7 kbar and ~530–570℃ (Figure 16a). We suggest that the late non-coaxial shearing at *LP* conditions could be responsible for the observed differences in metamorphic record and, locally, for an almost complete obliteration of the *HP* event products. The *LP* overprint is best recorded in sample PK033, which contains garnet with ilmenite forming sigmoidal inclusion trails and staurolite preserved in the rims of garnet grains. The observations testify to a low-*P* origin for garnet in this sample and also demonstrate their syntectonic character. In contrast, the

coarse-grained sample PK028 shows barely noticeable traces of deformation structures developed at low pressure and, thus, the *LP* overprint is weak. These observations also point to the heterogeneous nature of the late non-coaxial shearing in the KMB.

The crustal complexes of the Bohemian Massif have been recently considered as having formed in response to underthrusting of the Saxothuringian crustal domain beneath the Teplá–Barrandian domain and their subsequent collision with the Brunovistulian microcontinent (e.g. Chopin et al., 2012; Mazur et al., 2012; Schulmann et al., 2009). This explanation was proposed for the Sudetes, which are located south of the Sudetic Boundary Fault (Figure 1). However, a similar model could be offered for the Fore-Sudetic Block, which hosts the KMB. Recent investigations indicate that crustal complexes of the Central Sudetes, including the KMB, may represent the easternmost extent of the Saxothuringian crust (e.g. Jastrzębski et al., 2020; Mazur et al., 2012; Oberc-Dziedzic et al., 2018; Szczepański et al., 2019; Tab aud et al., 2021). The KMB

**FIGURE 13** (a) Isochemical phase diagram for sample PK033 calculated for the core composition of the investigated garnet. (b) Modelled isopleths for core composition of garnet shown for mole fraction of almandine (red), grossular (blue), and spessartine (purple). Mole fraction isopleths are shaded using 0.01 intervals. Additionally are shown stability fields of garnet, clinopyroxene, chloritoid, lawsonite, plagioclase, staurolite, ilmenite and rutile. (c) Compositional isopleths of $Si^{4+}$ in K-white mica (pfu, based on 11 oxygens). (d) Modelled isopleths for rim composition of garnet shown for mole fraction of almandine (red), grossular (blue), and spessartine (purple) with shading that spans two contour intervals of 0.01 mole fraction. Stability fields of garnet, clinopyroxene, chloritoid, lawsonite, plagioclase, ilmenite and rutile are additionally shown. (e) Compositional isopleths of the #Mg in staurolite. Yellow areas mark the intersection of isopleths

(a)

Ms+Cpx+Cld+Rt+Lws          Grt+Ms+Cpx+Cld+Rt+Lws

Chl+Ms+Cpx+Cld+Rt+Lws                    17
                                                    Grt+Ms+Pg+
Chl+Ms+Pg+Cpx+Cld+Rt+Lws              16        Cld+Rt

Chl+Ms+Pg+Cld+Rt+Lws

                    Grt+Chl+Ms+Pg+          Grt+Chl+Ms+
                    Cld+Rt+Lws              Pg+Cld+Rt

                                       Grt+Chl
                                       +Ms+Pg+      Grt+Bt+Chl
                                       Rt          +Ms+Pg+
                                                   Rt

Grt+Chl+Ms+Pg+
Cld+Rt+Spn          4
            3
        1   2   8   5
            7   9   10
    6           12  13
                    15
            11  14

(b) — Cpx in, Grt in, Lws in, Cld in, Ilm in, Rt in, Pl in, St in; contours 17.2, 66.3, 12.4

(c) contours 3.5, 3.3, 3.28, 3.12, 3.08, 3.06, 3.04

(d) — Cpx in, Grt in, Lws in, Cld in, Ilm in, Rt in, Pl in; contours 10.0, 12.6, 70.7

(e) St in; contours 0.1, 0.12, 0.14

1. Grt + Chl + Ms + Pg + Rt + Spn
2. Grt + Chl + Ms + Pg + Ilm + Rt + Spn
3. Grt + Chl + Ms + Pg + Ilm + Rt
4. Grt + Bt + Chl + Ms + Pg + Ilm + Rt
5. Grt + Bt + Chl + Ms + Ilm + Rt
6. Grt + Chl + Ms + Rt + Spn
7. Grt + Chl + Ms + Ilm + Rt + Spn
8. Grt + Chl + Ms + Ilm + Rt
9. Grt + Chl + Ms + Ilm
10. Grt + Bt + Chl + Ms + Ilm
11. Pl + Bt + Chl + Ms + Ilm
12. Pl + Grt + Chl + Ms + Ilm
13. Pl + Grt + Bt + Chl + Ms + Ilm
14. Pl + Grt + Bt + Chl + Ms + Ilm + Cld
15. Pl + Grt + Bt + Chl + Ms + Ilm + St
16. Grt + Chl + Ms + Pg + Cpx + Cld + Rt + Lws
17. Grt + Chl + Ms + Cpx + Cld + Rt + Lws
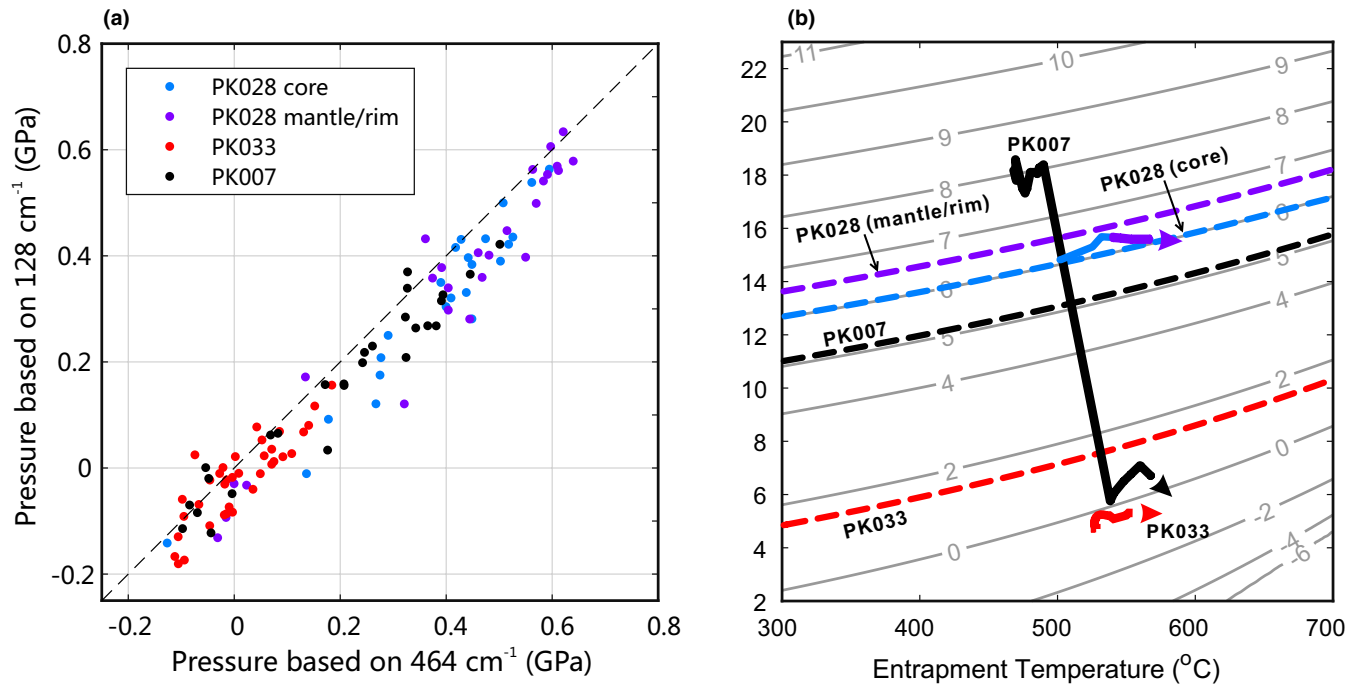
**FIGURE 14** (a) Quartz inclusion residual pressures converted from Raman spectroscopic data of the 128 and 464 cm⁻¹ bands. Experimental calibration from Schmidt and Ziemann (2000) is used assuming quartz inclusions to be under hydrostatic stress condition. (b) Calculated quartz inclusion pressure isomekes for observed garnet composition as host. The background isopleths show the calculated residual quartz inclusion pressures as a function of entrapment P-T conditions. The maximal quartz inclusion pressures from (a) are used to obtain the entrapment P for each sample. Additionally shown are P-T paths reconstructed based on garnet zoning. The discrepancy between the entrapment pressures of quartz inclusion and the pressures based on garnet growth modelling is within 2 kbar for sample PK033 and PK028. For sample PK007, the peak pressure predicted from garnet growth modelling is ca. 5~6 kbar higher than the quartz entrapment pressure

can be considered as a portion of the Saxothuringian crust that has experienced metamorphism typical of subduction zones. Taking into account available tectonic models, we suggest that the observed metamorphic record most probably resulted from collision and underthrusting of the Saxothuringian crust below the Brunovistulian microcontinent (Figure 16b). The record of this collisional event can be found in the Brunovistulian domain as relatively abundant Upper Devonian supra-subduction metavolcanics, which are interpreted as relics of a volcanic arc, and quartzitic metasandstones exposed in the East Sudetes, which might have been derived from erosion of supra-subduction volcanic complexes (Janoušek et al., 2014; Szczepański, 2007). The underthrusted and mechanically weakened Saxothuringian crust was folded in front of the rigid Brunovistulian intender as depicted by the numerical models of Maierová et al. (2014). To describe the origin and structure of the crustal complexes exposed in the Bohemian Massif, the authors proposed either gravity-driven or fold-dominated deformation scenarios. In the first scenario, high heat production and a relatively slow convergence rate of colliding crustal blocks led to high-T conditions of metamorphism, mechanical weakening of the material resulting in gravitational instability, and, as a consequence, vertical

exchange of crustal complexes. In the second scenario, low heat production due to a low concentration of felsic rocks in the underthrusted crust coupled with a rapid convergence resulted in crustal-scale folding and extrusion of the rocks even from the low crustal levels. In such scenario, the analysed rock complexes may have experienced cold extrusion from depth corresponding to pressures of ~18 kbar and temperatures below ~500℃ (Maierová et al., 2014). This generally seems to be the case of the crustal complexes located east of the Góry Sowie Massif, including the KMB. The numerical model of Maierová et al. (2014) shows that folding is the main mechanism responsible for exhumation of crustal material in the fold-dominated scenario. This is in agreement with our observations indicating that folding in the KMB already started during the HP episode, as shown by small-scale folds preserved in garnet porphyroblasts from sample PK028, and continued in the shallow crustal levels, as shown by microstructures preserved in the PK007 sample. The thermodynamic modelling presented in our study established that the non-coaxial shearing recognized in the inspected samples operated at pressures of ~3–5 kbar. Hence, the folding processes were also active after extensive exhumation, potentially driven by the mechanical instability due to the overthickened rock complexes.
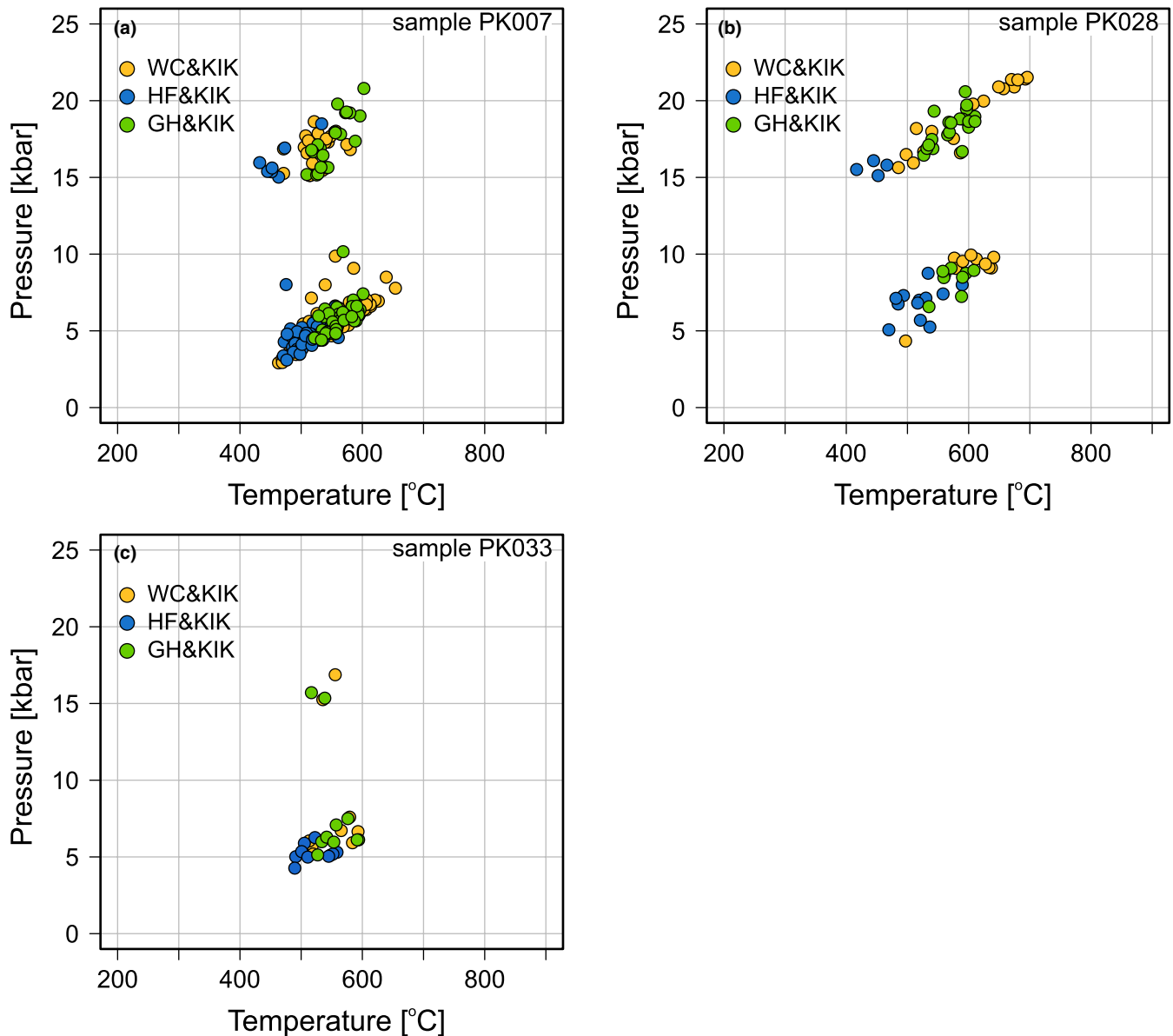
**FIGURE 15** Results of geothermobarometric calculations for sample: (a) PK007, (b) PK028 and (c) PK033. KIK - $Si^{4+}$ in phengite geobarometer (Kamzolkin et al., 2016). WC - $Ti^{4+}$ in white mica geothermometer (Wu & Chen, 2015). Garnet-muscovite geothermometer in calibration of HF - Hynes and Forest (1988) and GH - Green and Hellmann (1982)

Summing up, we postulate that the KMB may represent an allochtonous fragment of the Saxothuringian domain. Most probably owing to relatively fast convergence rate and low heat production, this portion of the Saxothuringian crust underwent folding and cold extrusion from below the Teplá–Barrandian in front of a rigid indenter represented by the Brunovistulian microcontinent (Figure 16).

## 8.2 | Stability and preservation of high-*P* quartz inclusions in garnet

The recovered entrapment pressures based on quartz-in-garnet Raman barometry for sample PK028 and PK033 are

very close to the predicted pressures from thermodynamic modelling being within ~1–2 kbar (Figure 14). However, for sample PK007, the maximal entrapment pressure recovered by quartz inclusions is ~4–5 kbar lower than the peak metamorphic pressure recovered by thermodynamic modelling of garnet growth (see Figure 14). It is noted that we have imposed strict selection rules and thick sections in searching for the quartz inclusions: for example, the inclusions are isolated and close to spherical with radii less than 2 to 5 μm and depth more than two to three times the inclusion radius (Mazzucchelli et al., 2018; Zhong et al., 2019). Therefore, residual pressure modifications due to inclusion shape and proximity to thin-section surface are not likely to be responsible for the systematic lower entrapment pressure and the

**(a)**



**(b)**
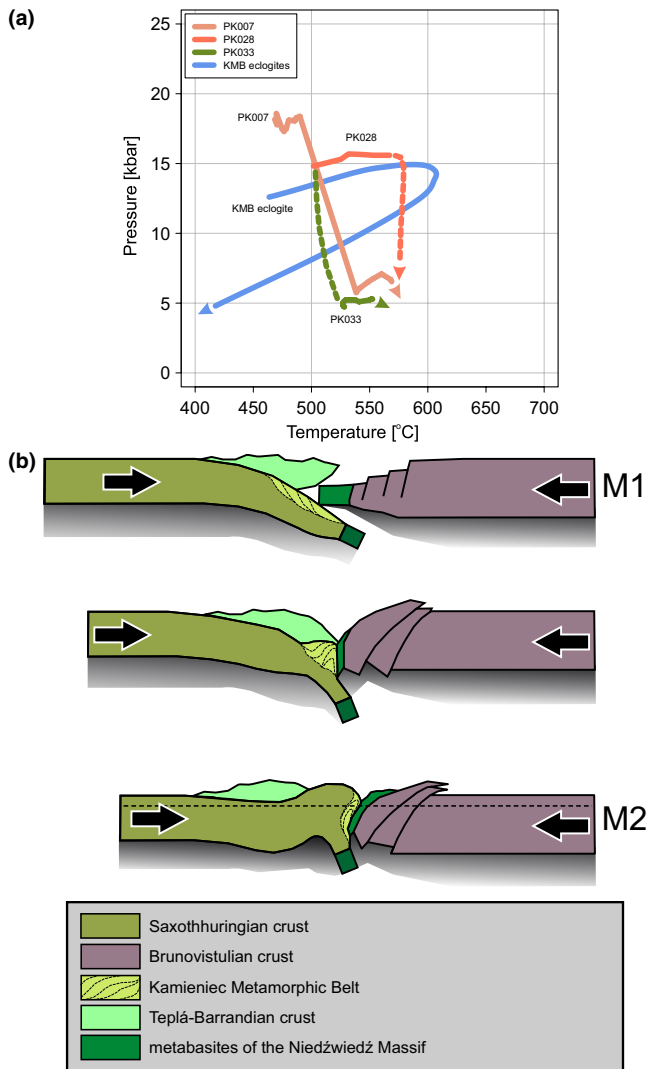


**FIGURE 16** (a) Summary of inferred P-T paths calculated for the investigated samples. The solid lines mark the part of the P–T path reconstructed based on garnet composition, while dashed lines mark the P–T path portions reconstructed based on other minerals (mainly white mica composition); The solid blue line shows the P–T path reported for *HP* eclogites from the Kamieniec Metamorphic Belt (Bakun-Czubarow, 1998); (b) Tectonic model (not to scale) showing a possible mechanism of exhumation of the KMB mica schists. The dashed line illustrates the present erosion level

wide scattering of the measured residual inclusion pressure shown in Figure 14.

The effect of elastic anisotropy of quartz inclusion on residual stress has been studied in, for example, Murri et al. (2018), Bonazzi et al. (2019), and Zhong et al., (2021). For a quartz inclusion entrapped in almandine garnet at ~15 kbar and 500℃, the residual differential stress $\sigma_1–\sigma_2$ of the quartz inclusion after exhumation is predicted to be minor (<1 kbar). Because the residual stress state of quartz inclusion is relatively close to hydrostatic, the applications of

experimental calibration between Raman shift and pressure (Schmidt & Ziemann, 2000), and the 1D isotropic elastic model (Guiraud & Powell, 2006) are suitable in this case. Therefore, elastic anisotropy of quartz inclusions alone cannot fully explain the observed discrepancy between the pressure estimates based on the Raman spectroscopy and mineral equilibria.

Similar magnitudes of pressure discrepancy have been reported for high-*P* rocks in, for example, Stak eclogite (Himalaya), Kulet whiteschist (Kazakhstan) etc. (Korsakov et al., 2010; Kouketsu et al., 2016). It has been inferred that viscous creep may have occurred during isothermal decompression at high temperature (>750~800℃), which partially relaxed the residual quartz inclusion pressure (Zhong et al., 2018). However, in our case the maximal temperature recorded is less than 550℃. The extrapolation of the almandine garnet flow law to such low-*T* conditions yields unrealistically long characteristic viscous relaxation times (>$10^3$ Ma) for GPa level differential stress (Dabrowski et al., 2015; Karato et al., 1995; Zhong et al., 2020). Therefore, it is unlikely that the residual stress relaxation observed in our study can be related to a time-dependent viscous creep of the garnet host.

The effect of garnet growth overstepping has been studied in, for example, Spear et al., (2014) and Castro and Spear (2017) to explain the discrepancy between the *P–T* estimates based on equilibrium thermodynamic modelling and Raman elastic barometry. In these cases, the pressure corresponding to the intersection of garnet compositional isopleth based on equilibrium model is generally lower than the Raman barometry results. In our sample PK007, it is the opposite in that the Raman barometry results are lower than the intersecting pressure of garnet compositional isopleths. For sample PK033 and PK028, the intersecting pressure of garnet compositional isopleths is ~2–3 kbar and ~1–2 kbar lower than the predicted entrapment pressure of quartz inclusion respectively. This degree of pressure discrepancy is similar to the reported values in Spear et al., (2014). The same sized discrepancy in the order of 2 kbar has also been reported in Thomas and Spear (2018), where the experimentally synthesized garnet shows a higher entrapment condition based on quartz inclusions than the imposed experimental pressure condition.

The samples studied here all exhibit strong shearing deformation. Although garnet is a rigid mineral that has high yield strength, it has been demonstrated to exhibit plastic behaviour under high differential stress at ~600℃ (Hawemann et al., 2019). A potential alternative explanation for the large pressure discrepancy for PK007 is that the externally imposed shear deformation after the formation of garnet porphyroblasts may result in a partial release of the overpressure in quartz inclusions during decompression (quartz pressure is reset). This may partially be supported by the presence of grains with negative Raman shift (negative pressure) in all the three investigated samples (Figure 14a). The peak negative

pressures of these samples approach ~1.5–1.8 kbar. Its magnitude is above the uncertainty of Raman spectroscopy (<0.2 kbar). It is speculated that pressure release may have occurred during the syntectonic isothermal decompression process accompanied with shear deformation. If this is true, the quartz inclusion pressure may potentially have been reset to lower pressure condition where the elastic isomeke corresponds to a negative value (Kouketsu et al., 2014). Further investigation on, for example, dislocation density around quartz inclusions in garnet could be performed to confirm if this is the case. Here, it does not influence the conclusion that the rock has undergone high-*P* event due to the other evidences pointing to high-*P* condition, for example, the high $Si^{4+}$ content in white mica, equilibrium modelling of garnet growth, and the high residual quartz pressure from sample PK028.

Another potential explanation for the lower quartz entrapment pressure recovered from sample PK007 is that most quartz inclusions from this sample are found in the garnet mantle and rim. The garnet grains are typically small (<0.4 mm) so that it is difficult to distinguish whether the quartz inclusions are from the 'true' core part or the 'apparent' core part by cutting the garnet grain through the mantle or rim. Quartz inclusions in the core part of the observed small garnet grains are rare. Therefore, it is also possible that most of the quartz inclusions obtained from sample PK007 have been measured from the garnet mantle and rim (or apparent garnet core in 2D section due to the cutting plane not passing through the garnet core), which were formed after the decompression as shown in Figure 14. If this is the case, the recovered entrapment pressure for sample PK007 may only represent the decompressed value during or after exhumation.

## ACKNOWLEDGEMENTS

## DATA AVAILABILITY STATEMENT

The data that supports the findings of this study are available in the supplementary material of this article.

## ORCID

*Jacek Szczepański* 🆔 https://orcid.org/0000-0001-9087-8164
*Xin Zhong* 🆔 https://orcid.org/0000-0002-2831-9625
*Marcin Dąbrowski* 🆔 https://orcid.org/0000-0003-0309-8050

## REFERENCES

Achramowicz, S., Muszynski, A., & Schliestedt, M. (1997). The north-easternmost eclogite occurrence in the Saxothuringian Zone, West Sudetes (Poland). *Chemie Der Erde-Geochemistry*, *57*(1), 51–61.

Aguilar, C., Štípská, P., Chopin, F., Schulmann, K., Pitra, P., Závada, P., Hasalová, P., & Martelat, J.-E. (2020). Syndeformational melt percolation through a high-pressure orthogneiss and the exhumation of a subducted continental wedge (Orlica-Śnieżnik Dome, NE Bohemian Massif). *International Journal of Earth Sciences*, *109*(4), 1213–1246. https://doi.org/10.1007/s00531-020-01838-4

Airaghi, L., Lanari, P., de Sigoyer, J., & Guillot, S. (2017). Microstructural vs compositional preservation and pseudomorphic replacement of muscovite in deformed metapelites from the Longmen Shan (Sichuan, China). *Lithos*, *282–283*, 262–280. https://doi.org/10.1016/j.lithos.2017.03.013

Aleksandrowski, P., & Mazur, S. (2002). Collage tectonics in the northeasternmost part of the Variscan Belt; the Sudetes, Bohemian Massif. *Palaeozoic Amalgamation of Central Europe*, *201*, 237–277. https://doi.org/10.1144/GSL.SP.2002.201.01.12

Angel, R. J., Alvaro, M., Miletich, R., & Nestola, F. (2017). A simple and generalised P-T–V EoS for continuous phase transitions, implemented in EosFit and applied to quartz. *Contributions to Mineralogy and Petrology*, *172*(5), 29. https://doi.org/10.1007/s00410-017-1349-x

Bakun-Czubarow, N. (1998). Ilmenite-bearing ecologites of the West Sudetes -their geochemistry and mineral chemistry. *Archiwum Mineralogiczne*, *51*(1–2), 29–110.

Berman, R. G. (1988). Internally-consistent thermodynamic data for minerals in the system $Na_2O$-$K_2O$-CaO-MgO-FeO-$Fe_2O_3$-$Al_2O_3$-$SiO_2$-$TiO_2$-$H_2O$-$CO_2$. *Journal of Petrology*, *29*(2), 445–522. https://doi.org/10.1093/petrology/29.2.445

Bonazzi, M., Tumiati, S., Thomas, J. B., Angel, R. J., & Alvaro, M. (2019). Assessment of the reliability of elastic geobarometry with quartz inclusions. *Lithos*, *350–351*, 105201. https://doi.org/10.1016/j.lithos.2019.105201

Castro, A. E., & Spear, F. S. (2017). Reaction overstepping and re-evaluation of peak P-T conditions of the blueschist unit Sifnos, Greece: Implications for the Cyclades subduction zone. *International Geology Review*, *59*(5–6), 548–562. https://doi.org/10.1080/00206814.2016.1200499

Catlos, E. J., Lovera, O. M., Kelly, E. D., Ashley, K. T., Harrison, T. M., & Etzel, T. (2018). Modeling high-resolution pressure-temperature paths across the himalayan main central thrust (Central Nepal): Implications for the dynamics of collision. *Tectonics*, *37*(8), 2363–2388. https://doi.org/10.1029/2018TC005144

Chatterjee, N. D. (1976). Margarite stability and compatibility relations in the system CaO-$Al_2O_3$-$SiO_2$-$H_2O$ as a pressure-temperature indicator. *American Mineralogist*, *61*, 699–709.

Chopin, F., Schulmann, K., Skrzypek, E., Lehmann, J., Dujardin, J. R., Martelat, J. E., Lexa, O., Corsini, M., Edel, J. B., Štípská, P., & Pitra, P. (2012). Crustal influx, indentation, ductile thinning and gravity redistribution in a continental wedge: Building a Moldanubian mantled gneiss dome with underthrust Saxothuringian material (European Variscan belt). *Tectonics*, *31*(1), https://doi.org/10.1029/2011TC002951

Chu, H., Wei, C., & Su, S. (2009). Phase equilibria of HP–UHP mica-schists in Jiangling, Eastern Dabieshan orogen. *Progress in Natural Science*, *19*(8), 973–982. https://doi.org/10.1016/j.pnsc.2008.12.004

Coggon, R., & Holland, T. J. B. (2002). Mixing properties of phengitic micas and revised garnetphengite thermobarometers. *Journal of Metamorphic Geology*, *20*(7), 683–696. https://doi.org/10.1046/j.1525-1314.2002.00395.x

Cruciani, G., Franceschelli, M., Massonne, H.-J., Carosi, R., & Montomoli, C. (2013). Pressure–temperature and deformational evolution of high-pressure metapelites from Variscan NE Sardinia, Italy. *Lithos*, *175–176*, 272–284. https://doi.org/10.1016/j.lithos.2013.05.001

Dabrowski, M., Powell, R., & Podladchikov, Y. (2015). Viscous relaxation of grain-scale pressure variations. *Journal of Metamorphic Geology*, *33*(8), 859–868. https://doi.org/10.1111/jmg.12142

de Capitani, C., & Petrakakis, K. (2010). The computation of equilibrium assemblage diagrams with Theriak/Domino software. *American Mineralogist*, *95*(7), 1006–1016. https://doi.org/10.2138/am.2010.3354

Droop, G. T. R. (1987). A general equation for estimating Fe (super 3+) concentrations in ferromagnesian silicates and oxides from microprobe analyses, using stoichiometric criteria. *Mineralogical Magazine*, *51*(361), 431–435.

Dziedzicowa, H. (1973). Mineral parageneses in metamorphic bentonite deposits within the Fore-Sudetic Block. *Bulletin de l'Academie polonaise des sciences. Serie des sciences de la terre*, *21*(2), 99–109.

Dziedzicowa, H. (1987). Rozwój strukturalny i metamorfizm we wschodnim obrzeżeniu gnejsów Gór Sowich. *Acta Univ. Wrat. Prace Geol.-Min*, *10*, 221–247.

Evans, T. P. (2004). A method for calculating effective bulk composition modification due to crystal fractionation in garnet-bearing schist; implications for isopleth thermobarometry. *Journal of Metamorphic Geology*, *22*(6), 547–557. https://doi.org/10.1111/j.1525-1314.2004.00532.x

Franke, W., Cocks, L. R. M., & Torsvik, T. H. (2017). The Palaeozoic Variscan oceans revisited. *Gondwana Research*, *48*, 257–284. https://doi.org/10.1016/j.gr.2017.03.005

Franke, W., Żelaźniewicz, A., Porębski, S. J., & Wajspyrch, B. (1993). Saxothuringian Zone in Germany and Poland; differences and common features. *Geologische Rundschau*, *82*(3), 583–599. https://doi.org/10.1007/BF00212418

Gaidies, F., Abart, R., De Capitani, C., Schuster, R., Connolly, J. A. D., & Reusser, E. (2006). Characterization of polymetamorphism in the Austroalpine basement east of the Tauern Window using garnet isopleth thermobarometry. *Journal of Metamorphic Geology*, *24*(6), 451–475. https://doi.org/10.1111/j.1525-1314.2006.00648.x

Gaidies, F., de Capitani, C., & Abart, R. (2008). THERIA_G: A software program to numerically model prograde garnet growth. *Contributions to Mineralogy and Petrology*, *155*(5), 657–671. https://doi.org/10.1007/s00410-007-0263-z

George, F. R., & Gaidies, F. (2017). Characterisation of a garnet population from the Sikkim Himalaya: Insights into the rates and mechanisms of porphyroblast crystallisation. *Contributions to Mineralogy and Petrology*, *172*(7), 57. https://doi.org/10.1007/s00410-017-1372-y

Gomez-Pugnaire, M. T., Visona, D., & Franz, G. (1985). Kyanite, margarite and paragonite in pseudomorphs in amphibolitized eclogites from the Betic Cordilleras. *Spain. Chemical Geology*, *50*(1–3), 129–141. https://doi.org/10.1016/0009-2541(85)90116-0

Gréaux, S., & Yamada, A. (2014). P-V–T equation of state of $Mn_3Al_2Si_3O_{12}$ spessartine garnet. *Physics and Chemistry of Minerals*, *41*(2), 141–149. https://doi.org/10.1007/s00269-013-0632-2

Green, E., Holland, T., & Powell, R. (2007). An order-disorder model for omphacitic pyroxenes in the system jadeite-diopside-hedenbergite-acmite, with applications to eclogitic rocks. *American Mineralogist*, *92*(7), 1181–1189. https://doi.org/10.2138/am.2007.2401

Green, T., & Hellmann, P. (1982). Fe-Mg partitioning between coexisting garnet and phengite at high pressure, and comments on a garnetphengite geothermometer. *Lithos*, *15*, 253–266. https://doi.org/10.1016/0024-4937(82)90017-2

Guiraud, M., & Powell, R. (2006). P-V–T relationships and mineral equilibria in inclusions in minerals. *Earth and Planetary Science Letters*, *244*(3–4), 683–694. https://doi.org/10.1016/j.epsl.2006.02.021

Gunia, T., Chorowska, M., Dziedzicowa, H., Dumicz, M., Niskiewicz, J., Sachanbiński, M., & Wojciechowska, I. (1979). *New microfloristic localities in metamorphic rocks east of Niemcza*, Field Conference Reports, s. 63–77.

Hamelin, C., Brady, J. B., Cheney, J. T., Schumacher, J. C., Able, L. M., & Sperry, A. J. (2018). Pseudomorphs after Lawsonite from Syros, Greece. *Journal of Petrology*, *59*(12), 2353–2384. https://doi.org/10.1093/petrology/egy099

Hawemann, F., Mancktelow, N., Wex, S., Pennacchioni, G., & Camacho, A. (2019). Fracturing and crystal plastic behaviour of garnet under seismic stress in the dry lower continental crust (Musgrave Ranges, Central Australia). *Solid Earth*, *10*(5), 1635–1649. https://doi.org/10.5194/se-10-1635-2019

Holland, T. J. B., & Powell, R. (1998). An internally consistent thermodynamic data set for phases of petrological interest. *Journal of Metamorphic Geology*, *16*(3), 309–343. https://doi.org/10.1111/j.1525-1314.1998.00140.x

Holland, T., & Powell, R. (2003). Activity-composition relations for phases in petrological calculations: An asymmetric multicomponent formulation. *Contributions to Mineralogy and Petrology*, *145*(4), 492–501. https://doi.org/10.1007/s00410-003-0464-z

Hynes, A., & Forest, R. C. (1988). Empirical garnet-muscovite geothermometry in low-grade metapelites, Selwyn Range (Canadian Rockies). *Journal of Metamorphic Geology*, *6*(3), 297–309. https://doi.org/10.1111/j.1525-1314.1988.tb00422.x

Janoušek, V., Aichler, J., Hanžl, P., Gerdes, A., Erban, V., Žáček, V., Pecina, V., Pudilová, M., Hrdličková, K., Mixa, P., & Žáčková, E. (2014). Constraining genesis and geotectonic setting of metavolcanic complexes: A multidisciplinary study of the Devonian Vrbno Group (Hrubý Jeseník Mts., Czech Republic). *International Journal of Earth Sciences*, *103*(2), 455–483. https://doi.org/10.1007/s00531-013-0975-4

Jastrzębski, M., Żelaźniewicz, A., Budzyń, B., Sláma, J., & Konečny, P. (2020). Age constraints on the Pre-Variscan and Variscan thermal events in the Kamieniec Ząbkowicki Metamorphic belt (the Fore-Sudetic Block, SW Poland). *Annales Societatis Geologorum Poloniae*, *90*, 27–49. https://doi.org/10.14241/asgp.2020.05

Jeřábek, P., Konopásek, J., & Žáčková, E. (2016). Two-stage exhumation of subducted Saxothuringian continental crust records underplating in the subduction channel and collisional forced folding (Krkonoše-Jizera Mts., Bohemian Massif). *Journal of Structural Geology*, *89*, 214–229. https://doi.org/10.1016/j.jsg.2016.06.008

Józefiak, D. (2000). Geothermobarometry in staurolilte-grade mica schists from the southern part of the Niemcza-Kamieniec Metamorphic Complex (Fore-Sudetic Block, SW Poland). *Neues Jahrbuch Für Mineralogie - Abhandlungen*, *175*(3), 223–248.

Kamzolkin, V. A., Ivanov, S. D., & Konilov, A. N. (2016). Empirical phengite geobarometer: Background, calibration, and application.

*Geology of Ore Deposits*, *58*(8), 613–622. https://doi.org/10.1134/S1075701516080092

Karato, S., Wang, Z., Liu, B., & Fujino, K. (1995). Plastic deformation of garnets: Systematics and implications for the rheology of the mantle transition zone. *Earth and Planetary Science Letters*, *130*(1–4), 13–30. https://doi.org/10.1016/0012-821X(94)00255-W

Konrad-Schmolke, M., Handy, M. R., Babist, J., & O'Brien, P. J. (2005). Thermodynamic modelling of diffusion-controlled garnet growth. *Contributions to Mineralogy and Petrology*, *149*(2), 181–195. https://doi.org/10.1007/s00410-004-0643-6

Korsakov, A. V., Perraki, M., Zhukov, V. P., De Gussem, K., Vandenabeele, P., & Tomilenko, A. A. (2010). Is quartz a potential indicator of ultrahigh-pressure metamorphism? Laser Raman spectroscopy of quartz inclusions in ultrahigh-pressure garnets. *European Journal of Mineralogy*, *21*(6), 1313–1323. https://doi.org/10.1127/0935-1221/2009/0021-2006

Kouketsu, Y., Hattori, K., Guillot, S., & Rayner, N. (2016). Eocene to Oligocene retrogression and recrystallization of the Stak eclogite in northwest Himalaya. *Lithos*, *240–243*, 155–166. https://doi.org/10.1016/j.lithos.2015.10.022

Kouketsu, Y., Nishiyama, T., Ikeda, T., & Enami, M. (2014). Evaluation of residual pressure in an inclusion-host system using negative frequency shift of quartz Raman spectra. *American Mineralogist*, *99*(2–3), 433–442. https://doi.org/10.2138/am.2014.4427

Maierová, P., Lexa, O., Schulmann, K., & Štípská, P. (2014). Contrasting tectono-metamorphic evolution of orogenic lower crust in the Bohemian Massif: A numerical model. *Gondwana Research*, *25*(2), 509–521. https://doi.org/10.1016/j.gr.2012.08.020

Martin, L. A. J., Hermann, J., Gauthiez-Putallaz, L., Whitney, D. L., Vitale Brovarone, A., Fornash, K. F., & Evans, N. J. (2014). Lawsonite geochemistry and stability - implication for trace element and water cycles in subduction zones. *Journal of Metamorphic Geology*, *32*(5), 455–478. https://doi.org/10.1111/jmg.12093

Mazur, S., Aleksandrowski, P., & Szczepański, J. (2005). The presumed Tepla-Barrandian/Moldanubian terrane boundary in the Orlica Mountains (Sudetes, Bohemian Massif): Structural and petrological characteristics. *Lithos*, *82*(1–2), 85–112.

Mazur, S., & Józefiak, D. (1999). Structural record of Variscan thrusting and subsequent extensional collapse in the mica schists from vicinities of Kamieniec Ząbkowicki, Sudetic foreland. *SW Poland. Annales Societatis Geologorum Poloniae*, *69*(1–2), 1–26.

Mazur, S., Kröner, A., Szczepański, J., Turniak, K., Hanžl, P., Melichar, R., Rodionov, N. V., Paderin, I., & Sergeev, S. A. (2010). Single zircon U/Pb ages and geochemistry of granitoid gneisses from SW Poland: Evidence for an Avalonian affinity of the Brunian microcontinent. *Geological Magazine*. https://doi.org/10.1017/S001675680999080X

Mazur, S., & Puziewicz, J. (1995). Deformation and metamorphism of rock series east of the Góry Sowie Block - new data and interpretations, (in Polish, English summary). *Przegląd Geologiczny*, *43*, 786–793.

Mazur, S., Szczepański, J., Turniak, K., & McNaughton, N. J. (2012). Location of the Rheic suture in the eastern Bohemian Massif: Evidence from detrital zircon data. *Terra Nova*, *24*(3), 199–206. https://doi.org/10.1111/j.1365-3121.2011.01053.x

Mazur, S., Turniak, K., Szczepański, J., & McNaughton, N. J. (2015). Vestiges of Saxothuringian crust in the Central Sudetes, Bohemian Massif: Zircon evidence of a recycled subducted slab provenance. *Gondwana Research*, *27*(2), 825–839. https://doi.org/10.1016/j.gr.2013.11.005

Mazzucchelli, M. L., Burnley, P., Angel, R. J., Morganti, S., Domeneghetti, M. C., Nestola, F., & Alvaro, M. (2018). Elastic geothermobarometry: Corrections for the geometry of the host-inclusion system. *Geology*, *46*(3), 231–234. https://doi.org/10.1130/G39807.1

Milani, S., Nestola, F., Alvaro, M., Pasqual, D., Mazzucchelli, M. L., Domeneghetti, M. C., & Geiger, C. A. (2015). Diamond–garnet geobarometry: The role of garnet compressibility and expansivity. *Lithos*, *227*, 140–147. https://doi.org/10.1016/j.lithos.2015.03.017

Moynihan, D. P., & Pattison, D. R. M. (2013). An automated method for the calculation of *P-T* paths from garnet zoning, with application to metapelitic schist from the Kootenay Arc, British Columbia, Canada. *Journal of Metamorphic Geology*, *31*(5), 525–548. https://doi.org/10.1111/jmg.12032

Murri, M., Mazzuchelli, M., Campomenosi, N., Korsakov, A. V., Prencipe, M., Mihailova, B., Scambelluri, M., Angel, R. J., & Alvaro, M. (2018). Raman elastic geobarometry for anisotropic mineral inclusions. *American Mineralogist*, https://doi.org/10.2138/am-2018-6625CCBY

Negulescu, E., Sabau, G., & Massonne, H.-J. (2009). Chloritoid-Bearing Mineral Assemblages in High-Pressure Metapelites from the Bughea Complex, Leaota Massif (South Carpathians). *Journal of Petrology*, *50*(1), 103–125. https://doi.org/10.1093/petrology/egn075

Nowak, I. (1998). Polyphase exhumation of eclogite-bearing high-pressure mica schists from the Fore-Sudetic Block, SW Poland. *Geologia Sudetica*, *31*(1), 3–31.

Oberc-Dziedzic, T., Klimas, K., Kryza, R., & Fanning, C. (2003). SHRIMP U-Pb zircon geochronology of the Strzelin gneiss, SW Poland: Evidence for a neoproterozoic thermal event in the Fore-Sudetic Block, Central European Variscides. *International Journal of Earth Sciences*, *92*(5), 701–711. https://doi.org/10.1007/s00531-003-0345-8

Oberc-Dziedzic, T., Kryza, R., Madej, S., & Pin, C. (2018). The Saxothuringian Terrane affinity of the metamorphic Stachów Complex (Strzelin Massif, Fore-Sudetic Block, Poland) inferredfrom zircon ages. *Geological Quarterly*, *62*(2), https://doi.org/10.7306/gq.1405

Oliver, G., Corfu, F., & Krogh, T. (1993). U-Pb ages from SW Poland - Evidence for a Caledonian suture zone between Baltica and Gondwana. *Journal of the Geological Society*, *150*(Part 2), 355–369. https://doi.org/10.1144/gsjgs.150.2.0355

Orozbaev, R., Hirajima, T., Bakirov, A., Takasu, A., Maki, K., Yoshida, K., Sakiev, K., Bakirov, A., Hirata, T., Tagiri, M., & Togonbaeva, A. (2015). Trace element characteristics of clinozoisite pseudomorphs after lawsonite in talc-garnetchloritoid schists from the Makbal UHP Complex, northern Kyrgyz Tian-Shan. *Lithos*, *226*, 98–115. https://doi.org/10.1016/j.lithos.2014.10.008

Philippon, M., Gueydan, F., Pitra, P., & Brun, J.-P. (2013). Preservation of subduction-related prograde deformation in lawsonite pseudomorph-bearing rocks. *Journal of Metamorphic Geology*, *31*(5), 571–583. https://doi.org/10.1111/jmg.12035

Pietranik, A., Storey, C., & Kierczak, J. (2013). The Niemcza diorites and moznodiorites (Sudetes, SW Poland): A record of changing geotectonic setting at ca. 340 Ma. *Geological Quarterly*, *57*(2), https://doi.org/10.7306/gq.1084

Poli, S., & Schmidt, M. W. (1995). $H_2O$ transport and release in subduction zones: Experimental constraints on basaltic and andesitic systems. *Journal of Geophysical Research: Solid Earth*, *100*(B11), 22299–22314. https://doi.org/10.1029/95JB01570

Schmidt, C., & Ziemann, M. A. (2000). In-situ Raman spectroscopy of quartz: A pressure sensor for hydrothermal diamond-anvil cell experiments at elevated temperatures. *American Mineralogist*, *85*(11–12), 1725–1734. https://doi.org/10.2138/am-2000-11-1216

Schulmann, K., & Gayer, R. (2000). A model for a continental accretionary wedge developed by oblique collision: The NE Bohemian Massif. *Journal of the Geological Society, London*, *157*(Part 2), 401–416. https://doi.org/10.1144/jgs.157.2.401

Schulmann, K., Konopásek, J., Janoušek, V., Lexa, O., Lardeaux, J.-M., Edel, J.-B., Štípská, P., & Ulrich, S. (2009). An Andean type Palaeozoic convergence in the Bohemian Massif. *Comptes Rendus Geosciences*, *341*(2–3), 266–286. https://doi.org/10.1016/j.crte.2008.12.006

Simakov, S., & Dolivo-Dobrovolsky, M. (2009). *PTQuick. Versions: 1.4.0.5 (PTQuick.exe), 1.4.0.9 (PTools.dll)*. Retrieved from http://dimadd.ru/en/Programs/ptquick.

Spear, F. S., Thomas, J. B., & Hallett, B. W. (2014). Overstepping the garnet isograd: A comparison of QuiG barometry and thermodynamic modeling. *Contributions to Mineralogy and Petrology*, *168*(3), 1059. https://doi.org/10.1007/s00410-014-1059-6

Steltenpohl, M. G., Cymerman, Z., Krogh, E. J., & Kunk, M. J. (1993). Exhumation of eclogitized continental basement during Variscan lithospheric delamination and gravitational collapse, Sudety Mountains, Poland. *Geology*, *21*(12), 1111–1114. https://doi.org/10.1130/0091-7613(1993)021<1111:EOECBD>2.3.CO;2

Szczepański, J. (2007). A vestige of an Early Devonian active continental margin in the East Sudetes (SW Poland) - evidence from geochemistry of the Jegłowa Beds, Strzelin Massif. *Geological Quarterly*, *51*(3), 271–284.

Szczepański, J., Anczkiewicz, R., & Kaszuba, G. (2019). Detrital zircon provenance of volcanosedimentary succession from the Kamieniec Metamorphic Belt (the Sudetes, SW Poland): Preliminary data. *Mineralogia - Special Papers*, *49*, 87.

Tabaud, A. S., Štípská, P., Mazur, S., Schulmann, K., Míková, J., Wong, J., & Sun, M. (2021). Evolution of a Cambro-Ordovician active margin in northern Gondwana: Geochemical and zircongeochronological evidence from the Góry Sowie metasedimentary rocks, Poland. *Gondwana Research*, *90*, 1–26. https://doi.org/10.1016/j.gr.2020.10.011

Thomas, J. B., & Spear, F. S. (2018). Experimental study of quartz inclusions in garnet at pressures up to 3.0 GPa: Evaluating validity of the quartz-in-garnet inclusion elastic thermobarometer. *Contributions to Mineralogy and Petrology*, *173(5), 42*, 1192-. https://doi.org/10.1007/s00410-018-1469-y

Tsuchiya, S., & Hirajima, T. (2013). Evidence of the lawsonite eclogite facies metamorphism from an epidote-glaucophane eclogite in the Kotsu area of the Sanbagawa belt, Japan. *Journal of Mineralogical and Petrological Sciences*, *108*(3), 166–171. https://doi.org/10.2465/jmps.121022b

Tsujimori, T., & Ernst, W. G. (2014). Lawsonite blueschists and lawsonite eclogites as proxies for palaeo-subduction zone processes: A review. *Journal of Metamorphic Geology*, *32*(5), 437–454. https://doi.org/10.1111/jmg.12057

Ueno, T. (2001). Lawsonite-bearing pelitic schists from the Sanbagawa metamorphic belt in the Ise area, eastern Kii Peninsula, central Japan. *Japanese Magazine of Mineralogical and Petrological Sciences*, *30*(6), 255–264. https://doi.org/10.2465/gkk.30.255

Vrijmoed, J. C., & Hacker, B. R. (2014). Determining P-T paths from garnet zoning using a brute-force computational method. *Contributions to Mineralogy and Petrology*, *167*(4), 997. https://doi.org/10.1007/s00410-014-0997-3

White, R. W., Powell, R., Holland, T. J. B., & Worley, B. A. (2000). The effect of $TiO_2$ and $Fe_2O_3$ on metapelitic assemblages at greenschist and amphibolite facies conditions: Mineral equilibria calculations in the system $K_2O-FeO-MgO-Al_2O_3-SiO_2-H_2O-TiO_2-Fe_2O_3$. *Journal of Metamorphic Geology*, *18*(5), 497–511. https://doi.org/10.1046/j.1525-1314.2000.00269.x

White, R. W., Powell, R., & Holland, T. J. B. (2007). Progress relating to calculation of partial melting equilibria for metapelites. *Journal of Metamorphic Geology*, *25*(5), 511–527. https://doi.org/10.1111/j.1525-1314.2007.00711.x

Whitney, D. L., & Evans, B. W. (2010). Abbreviations for names of rock-forming minerals. *American Mineralogist*, *95*(1), 185–187. https://doi.org/10.2138/am.2010.3371

Wu, C.-M., & Chen, H.-X. (2015). Calibration of a Ti-in-muscovite geothermometer for ilmenite- and $Al_2SiO_5$-bearing metapelites. *Lithos*, *212–215*, 122–127. https://doi.org/10.1016/j.lithos.2014.11.008

Zhong, X., Dabrowski, M., & Jamtveit, B. (2019). Analytical solution for the stress field in elastic halfspace with a spherical pressurized cavity or inclusion containing eigenstrain. *Geophysical Journal International*, *216*(2), 1100–1115. https://doi.org/10.1093/gji/ggy447

Zhong, X., Dabrowski, M., & Jamtveit, B. (2021). Analytical solution for residual stress and strain preserved in anisotropic inclusion entrapped in isotropic host. *Solid Earth*, *12*, 817–833.

Zhong, X., Moulas, E., & Tajčmanová, L. (2018). Tiny timekeepers witnessing high-rate exhumation processes. *Scientific Reports*, *8*(1), 2234. https://doi.org/10.1038/s41598-018-20291-7

Zhong, X., Moulas, E., & Tajčmanová, L. (2020). Post-entrapment modification of residual inclusion pressure and its implications for Raman elastic thermobarometry. *Solid Earth*, *11*(1), 223–240. https://doi.org/10.5194/se-11-223-2020

## SUPPORTING INFORMATION

Additional supporting information may be found online in the Supporting Information section.

Figure S1. X-Ray maps illustrating chemical zoning of a garnet porphyroblast from sample PK007. Comparison of Fe and Ti maps indicate that Grt1 (cores of inspected garnet grains) contains rutile, while Grt2 (rims of inspected garnet grains) comprise mostly ilmenite. Note the sharp variation of the chemical composition from Grt1 to Grt2, especially for Mn.

Figure S2. X-Ray maps illustrating chemical zoning of a garnet porphyroblast from sample PK007. Comparison of Fe and Ti maps indicate that Grt1 (cores of inspected garnet grains) contains rutile, while Grt2 (rims of inspected garnet grains) comprise mostly ilmenite.

Figure S3. SEM images of garnet grains from sample PK033. Note that inclusions in garnet grains are represented by ilmenite and staurolite. Ilmenite and staurolite are also present in the matrix of the inspected sample.

Figure S4. Isochemical phase diagram for sample PK007 calculated for the bulk rock composition. Mole fraction isopleths of almandine (red), grossular (blue), and spessartine

(purple) for Grt1 are shown. Orange line shows lower limit for garnet stability.

Figure S5. Isochemical phase diagram for sample PK007 calculated for the effective bulk rock composition after Grt1 growth. Mole fraction isopleths of almandine (red), grossular (blue), and spessartine (purple) are shown. Orange line shows the lower limit for garnet stability.

Figure S6. Isochemical phase diagram for sample PK028 calculated for the effective bulk rock composition. Mole fraction isopleths of almandine (red), grossular (blue), and spessartine (purple) are shown. Orange line shows the lower limit for garnet stability.

Figure S7. Changes of vol% of selected minerals along the modelled P-T path for sample PK028: (a) paragonite and K-white mica. (b) Garnet, clinopyroxene, plagioclase. (c) Rutile and ilmenite. (d) Modelled PT path, (e) compositional transect across garnet in sample PK028. Color circles are the garnet composition obtained using an electron microprobe; black lines show the smoothed fit of the electron microprobe data and are compositions used in the modeling program.

Figure S8. Isochemical phase diagram for sample PK033 calculated for the effective bulk rock composition. The measured garnet core isopleths are shown for mole fraction of almandine (red), grossular (blue), and spessartine (purple). Orange line shows lower limit for garnet stability.

Figure S9. Results of thermodynamic modeling for sample PK007 using fractionation model proposed by Evans (2004). Black circles mark intersection of garnet isopleths. (a) Garnet isopleths and phase stability limits calculated for the unfractionated rock composition and the core composition of garnet grains. (b) chloritoid stability field and isopleths for $X_{Mg}$ in chloritoid for unfractionated rock composition. (c) Garnet isopleths and garnet vol% isopleth calculated for end of Grt1 crystallization, (d) garnet isopleths and phase stability limits calculated for the onset of Grt2 crystallization. (e) Garnet isopleths and ilmenite stability limit calculated for end of Grt2 crystallization. (f) Si in white mica isopleths and reconstructed PT path.

Figure S10. Results of thermodynamic modeling using fractionation model proposed by Evans (2004) for sample PK028. Black circles mark intersection of garnet isopleths. (a) Garnet isopleths and (b) phase stability limits calculated for unfractionated rock composition and core of garnet grains. (c) Garnet isopleths and phase stability limits calculated for fractionated rock composition and garnet rims. (d) Si in white mica isopleths and two possible reconstructed P-T path.

Figure S11. Results of thermodynamic modeling using fractionation model proposed by Evans (2004) for sample PK033. Black circles mark intersection of garnet isopleths. (a) Garnet isopleths and phase stability limits calculated for unfractionated rock composition and core of garnet grains. (b) Garnet isopleths and phase stability limits calculated for fractionated rock composition and garnet mantle. (c) Garnet isopleths and phase stability limits calculated for fractionated rock composition and garnet rims. (d) Si in white mica isopleths, staurolite stability field and reconstructed P-T path.

Figure S12. Results of thermodynamic modeling using the brute force method proposed by Vrijmoed and Hacker (2014) for sample PK007.

Figure S13. Results of thermodynamic modeling using the brute force method proposed by Vrijmoed and Hacker (2014) for sample PK028.

Figure S14. Results of thermodynamic modeling using the brute force method proposed by Vrijmoed and Hacker (2014) for sample PK033.

Figure S15. Photomicrographs of quartz inclusions from sample PK028.

Table S1. Summary of Raman shifts and residual pressures for quartz inclusions from sample PK007.

Table S2. Summary of Raman shifts and residual pressures for quartz inclusions from sample PK028.

Table S3. Summary of Raman shifts and residual pressures for quartz inclusions from sample PK033.